Bulletin of Volcanology

Silicic conduits as supersized tuffisites: Clastogenic influences on shifting eruption styles at Cordón Caulle volcano (Chile)

--Manuscript Draft--

Manuscript Number:	BUVO-D-20-00088R1
Full Title:	Silicic conduits as supersized tuffisites: Clastogenic influences on shifting eruption styles at Cordón Caulle volcano (Chile)
Article Type:	Research Article
Corresponding Author:	C Ian Schipper Victoria University of Wellington NEW ZEALAND
Corresponding Author Secondary Information:	
Order of Authors:	C Ian Schipper
	Jonathan M. Castro
	Ben M. Kennedy
	Hugh Tuffen
	Jack Whattam
	Fabian B. Wadsworth
	Rebecca Paisley
	Rebecca H. Fitzgerald
	Emma Rhodes
	Lauren N. Schaefer
	Paul A. Ashwell
	Pablo Forte
	Gilles Seropian
	Brent V. Alloway
Funding Information:	
Abstract:	Understanding the processes that drive explosive-effusive transitions during large silicic eruptions is crucial to hazard mitigation. Conduit models usually treat magma ascent and degassing as a gradual, unidirectional progression from bubble nucleation through to magmatic fragmentation. However, there is growing evidence for the importance of bi-directional clastogenic processes that sinter fragmented materials into coherent clastogenic magmas. Bombs that were ejected immediately before the first emergence of lava in the 2011-2012 eruption at Cordón Caulle volcano (Chile) are texturally heterogeneous composite assemblages of welded pyroclastic material. Although diverse in density and appearance, SEM and X-Ray tomographic analysis show them all to have been formed by multi-generational viscous sintering of fine ash. Sintering created discrete clasts ranging from obsidian to pumice and formed a pervasive clast-supporting matrix that assembled these clasts into a conduit-sealing plug. An evaluation of sintering timescales reveals texturally disparate bomb components to represent only minutes of difference in residence time within the conduit. Permeability modeling indicates that the plug was an effective conduit seal, with outgassing potential – even from high-porosity regions – being limited by the inability of gas to flow across tendrils of densely sintered inter-clast matrix. Contrary to traditional perspectives, declining expressions of explosivity at the surface need not be preceded or accompanied by a decline in fragmentation efficiency. Instead, they result from tips in balance between the opposing processes of fragmentation and sintering that occur in countless cycles within volcanic conduits. These processes may be

	particularly enhanced at silicic fissure volcanoes, which have laterally extensive subsurface plumbing systems that require complex magma ascent pathways. The textures investigated here reveal the processes occurring within silicic fissures to be phenomenologically identical to those that have been inferred to occur in tuffisite veins: silicic conduits are essentially supersized examples of edifice-penetrating tuffisite veins.
Response to Reviewers:	Please see attached document: Schipper et al. Revisions.docx
Author Comments:	Dear Bulletin of Volcanology editorial board, We are pleased to submit for your consideration the manuscript: Silicic conduits as supersized tuffisites: Clastogenic influences on shifting eruption styles at Cordón Caulle volcano (Chile) This manuscript is the product of several years of analysis on eruption products from the 2011-2012 Cordón Caulle eruption. It contains data and interpretations that link transitions in eruption style to clastogenic processes occurring in the conduit. These are major current topics in volcanology, and we believe this work will be of wide interest to the readership of the Bulletin of Volcanology. We respectfully ask that Dr. Y. Moussallam not be assigned as the handling editor for this submission, due to conflicts of interest with the lead author. We thank you for considering our work for publication. With regards, Dr. C. Ian Schipper, on behalf of all co-authors

Silicic conduits as supersized tuffisites: Clastogenic influences on shifting eruption styles at Cordón Caulle volcano (Chile)

C. Ian Schipper[1]*, Jonathan M. Castro[2], Ben M. Kennedy[3], Hugh Tuffen[4], Jack Whattam[1], Fabian B. Wadsworth[5], Rebecca Paisley[6], Rebecca H. Fitzgerald[3], Emma Rhodes[3,7], Lauren N. Schaefer[3,8], Paul A. Ashwell[3,9], Pablo Forte[2,10], Gilles Seropian[3], Brent V. Alloway[11,12]

*corresponding author
ian.schipper@vuw.ac.nz
+64 (0)4 463 8197

[1] School of Geography, Environment and Earth Sciences, Victoria University of Wellington, PO Box 600, Wellington 6140, New Zealand
[2] Institute of Geosciences, Johannes Gutenberg University, Mainz, Germany
[3] Earth and Environment, University of Canterbury, Private Bag 4800, Christchurch, New Zealand
[4] Lancaster Environment Centre, Lancaster University, LA1 4YQ, UK
[5] Department of Earth Sciences, Durham University, Durham, DH1 3LE, UK
[6] Department of Earth and Planetary Sciences, McGill University,3450 Rue University, Montreal, Quebec H3A0E8, Canada
[7] Department of Earth Sciences, Uppsala University, Uppsala, Sweden
[8] U.S. Geological Survey, 1711 Illinois St., Golden, CO, 80401, USA
[9] Department of Chemical and Physical Sciences, University of Toronto, Mississauga, Ontario, L5L, Canada
[10] Instituto de Estudios Andinos, UBA-CONICET, Buenos Aires, Argentina
[11] School of Environment, The University of Auckland, Private Bag 92019, Auckland, New Zealand
[12] Núcleo Milenio Paleoclima, Centro de Estudios del Clima y la Resiliencia, and Departamento de Ciencias Ecológicas, Universidad de Chile, Santiago, Chile

Abstract

Understanding the processes that drive explosive-effusive transitions during large silicic eruptions is crucial to hazard mitigation. Conduit models usually treat magma ascent and degassing as a gradual, unidirectional progression from bubble nucleation through to magmatic fragmentation. However, there is growing evidence for the importance of bi-directional clastogenic processes that sinter fragmented materials into coherent clastogenic magmas. Bombs that were ejected immediately before the first emergence of lava in the 2011-2012 eruption at Cordón Caulle volcano (Chile) are texturally heterogeneous composite assemblages of welded pyroclastic material. Although diverse in density and appearance, SEM and X-Ray tomographic analysis show them all to have been formed by multi-generational viscous sintering of fine ash. Sintering created discrete clasts ranging from obsidian to pumice and formed a pervasive clast-supporting matrix that assembled these clasts into a conduit-sealing plug. An evaluation of sintering timescales reveals texturally disparate bomb components to represent only minutes of difference in residence time within the conduit. Permeability modeling indicates that the plug was an effective conduit seal, with outgassing potential – even from ~~low~~high-porosity regions – being limited by the inability of gas to flow across tendrils of densely sintered inter-clast matrix. Contrary to traditional perspectives, declining expressions of explosivity at the surface need not be preceded or accompanied by a decline in fragmentation efficiency. Instead, they result from tips in balance between the opposing processes of fragmentation and sintering that occur in

countless cycles within volcanic conduits. These processes may be particularly enhanced at silicic fissure volcanoes, which have laterally extensive subsurface plumbing systems that require complex magma ascent pathways. The textures investigated here reveal the processes occurring within silicic fissures to be phenomenologically identical to those that have been inferred to occur in tuffisite veins:~~;~~ silicic conduits are essentially ~~being~~ supersized examples of edifice-penetrating tuffisite veins.

Keywords: *Cordón Caulle, rhyolite, sintering, explosive-effusive transition*

1 Introduction

Silicic eruptions are among the most destructive of naturally occurring phenomena. Many undergo an explosive-to-effusive transition, when widespread pyroclast dispersal is followed by ~~relatively gentle~~ outpourings of lava (e.g., Eichelberger and Westrich 1981; Eichelberger et al. 1986; Adams et al. 2006; Castro and Gardner 2008). Transitions are generally thought to involve intrinsic shifts from closed-system degassing that promotes rapid magma ascent and fragmentation, to open-system degassing that promotes gas escape, slow magma ascent, and preservation of melt coherence (e.g., Taylor et al. 1983; Eichelberger et al. 1986; Newman et al. 1988; Degruyter et al. 2012). They can also be linked to extrinsic controls such as declining magma ascent rates driven by changes in conduit geometry or exhaustion of magma supply (Nguyen et al. 2014; Cassidy et al. 2018). Understanding these transitions is critical, as each marks a dramatic ~~decline~~ reduction in the footprint of an eruption's impact ~~footprint~~, and is a key milestone in hazard mitigation (Elissondo et al. 2016).

Fragmentation was long considered to be the defining feature of explosive eruptions (Eichelberger 1995) but there is now abundant evidence that fragmentation and explosivity are not synonymous. Localized fragmentation and shear fracturing in conduits can aid outgassing without ~~causing explosivity~~triggering explosive pyroclastic discharge to the surface (Gonnermann and Manga 2003; Rust et al. 2004). Transient fractures, or tuffisites, within and around magma-filled conduits can facilitate outgassing and overpressure modulation during predominantly effusive activity (Stasiuk et al. 1996; Tuffen et al. 2003; Tuffen et al. 2008; Cabrera et al. 2011; Castro et al. 2012; Kolzenburg et al. 2012; Cabrera et al. 2015; Kendrick et al. 2016; Saubin et al. 2016; Farquharson et al. 2017; Kolzenburg et al. 2019). Furthermore, even extensive fragmentation can be reversed by viscous sintering or welding of previously fragmented material (Quane and Russell 2005; Vasseur et al. 2013; Wadsworth et al. 2014; Gardner et al. 2017; Gardner et al. 2018, 2019; Heap et al. 2019). Still, existing conduit models seeking to describe explosive-effusive transitions require that some threshold for shifting activity be defined, and typically do so by investigating if ascending magma does or does not meet one of several criteria for fragmentation (Gonnermann and Manga 2003; Spieler et al. 2004; Degruyter et al. 2012; Nguyen et al. 2014; Cassidy et al. 2018).

A hindrance to understanding explosive-effusive transitions partly stems from the difficulty of identifying eruptive products that exemplify the physical state(s) of magma within conduits-in-transition (Adams et al. 2006). Explosive-effusive transitions appear as instantaneous events in the rock record (Taylor et al. 1983; Newman et al. 1988). Samples of early pyroclasts and later lavas provide insight about how end-member degassing regimes ultimately differed (Castro and Gardner 2008; Nguyen et al. 2014), but do not necessarily capture the crucial time window when eruption styles were dramatically shifting (Adams et al. 2006; Isgett et al. 2017). Furthermore, the effusive phase of silicic eruptions often produces vent-capping lava domes (c.f. Chaitén; Pallister et al. 2013)~~(c.f. Chaitén; Pallister et al., 2013)~~, which can ~~exacerbate erasure~~conceal ~~of~~ critical transitional eruption products. The 2011-2012 rhyolite eruption of Cordón Caulle volcano (Chile) provides an unprecedented opportunity to investigate the textural state of magma that was in the conduit during a closely observed explosive-effusive transition, ~~in~~ with~~which~~ lava that flowed efficiently away from its source vent (Tuffen et al., 2013).

1.1 The Cordón Caulle fissure, and eruptive transitions in 2011-2012

Cordón Caulle is a 15 km long and 4 km wide NW-SE trending fissure system within the <100 ka Puyehue-Cordón Caulle Volcanic Complex (PCCVC) in the Southern Chilean Andes. Cordón Caulle has been the site of the last three PCCVC eruptions, with rhyolite erupted from a variety of vents in 1921-22, 1960, and 2011-12 (Gerlach et al. 1988; Lara et al. 2006; Castro et al. 2013). The 1960 eruption was significant for having begun 38 hours after the Mw=9.5 Valdivia earthquake, and for creating a series of >20 vents. It has thus inspired analysis of the links between regional tectonics and eruption triggers, and demonstrated significant structural controls on silicic magma pathways in fissure systems (Lara et al. 2004; Delle Donna et al. 2010; Sawi and Manga 2018). The 2011-12 eruption began on June 4, 2011, with a Plinian eruption column that dispersed rhyolite tephra across Argentina and disrupted airspace throughout the southern hemisphere (Elissondo et al. 2016). It remains the largest terrestrial eruption to-date of the 21st century and is only the second eruption of rhyolite (after Chait~~e~~én, 2008) to have been directly observed by scientists.

The explosive-effusive transition at Cordón Caulle was protracted, occurring over many months. Plinian explosivity began on June 4-5, 2011, with an eruption column that reached >14 km (SERNAGEOMIN/OVDAS 2011). Effusive activity began when lava emerged from the vent on June 15, and continued until late 2012 (with endogenous lava advance continuing into 2013; Tuffen et al. 2013). But the style of explosivity changed character several times in the lead-up to lava emergence, and explosivity did not cease upon commencement of effusion (Castro et al. 2013; Castro et al. 2014).

Several key changes in eruption dynamics preceded the first emergence of lava at Cordón Caulle (Fig. 1C-D). June 7 saw a shift from tephra-depositing pyroclastic columns and density currents, to a period that included both sustained tephra emission and the ballistic ejection of bombs (Pistolesi et al. 2015). This onset of ballistic activity coincided with the beginning of intense uplift in the vent region, indicating that magma was starting to be emplaced as a laccolith in the shallow subsurface (Castro et al. 2016). Edifice inflation, tephra dispersal, and bomb ejection continued for 4-5 days, culminating in an intense period of ballistic activity on Jun 12-13, which was the last major event before lava emergence (SERNAGEOMIN/OVDAS 2011; Silva Parejas et al. 2012; Pistolesi et al. 2015; Castro et al. 2016).

Following lava emergence, the eruption entered into "hybrid" activity (Lara 2008; Castro et al. 2012; Silva Parejas et al. 2012; Castro et al. 2013) that included explosions and effusion from a common vent system. Hybrid activity lasted through early 2012, and progressively waned in intensity (Castro et al. 2013; Schipper et al. 2013). Despite these complex overlaps in style, the eruption can be understood to have undergone a protracted transition from predominantly explosive to predominantly effusive, with a commensurate decline in the eruption's tephra hazard footprint.

The fissural character of the Cordón Caulle system was less dramatically expressed at the surface in 2011-2012 than it had been in the previous two eruptions (e.g., Lara et al. 2004). All of the 2011-2012 explosive and effusive activity occurred from a relatively focused vent (apparent vent shifts in Fig.1A-F being a function of off-nadir MODIS viewing angles; Wang et al. 2011). However, the laterally extensive nature of the Cordón Caulle plumbing system was apparent in pre- and syn-eruptive deformation patterns captured in INSAR interferograms by Jay et al. (2014). They documented several deformation centres distributed along the structurally controlled NW-SE trend of Cordón Caulle, most notably two deflation centres 2-10 km from the 2011-2012 vent, that were active from May 8 – June 7, 2011. Furthermore, although the 2011-2012 vent shifts were not as dramatic in 1960, satellite images (Fig. 1G) and observations (Schipper et al. 2013) of hybrid activity showed concurrent activity of multiple sub-vents, also aligned in a NW-SE trend, at many points during the eruption.

We present textures of bombs from Cordón Caulle, predominantly focusing on those that were ejected during the high-energy ballistic episode that bridged initial (exclusively) explosive activity with subsequent (hybrid) effusive activity (SERNAGEOMIN/OVDAS 2011; Castro et al. 2013; Pistolesi et al. 2015). These texturally complex bombs have been noted and partially described by several authors (Castro et al. 2014; Pistolesi et al. 2015; Paisley et al. 2019a; Paisley et al. 2019b). We use bomb textures to gain insight into the state of magma within silicic fissures and their associated subvolcanic conduits in the lead-up to an explosive-effusive transition. We examine the processes that drive conduit closure and discuss the seeming dichotomy that opposing clastogenic processes (fragmentation versus sintering) can both prolong and extinguish explosivity from a constricting silicic system.

2 Samples and methods

Bombs were mapped and examined in vent-proximal and -distal field locations over five field seasons from 2013-2017. In November 2017, we carried out an aerial survey of the 2011-2012 Cordón Caulle vent and lava flow, using an XCam® camera fixed to a Cessna® 152 airplane, which collected a suite of high-resolution (7cm/pixel) orthophotos (Fig. 2B-C). Hundreds of bombs were examined in the field, 26 in collected hand samples, 21 in thin section, and 13 with X-Ray computed tomography (CT). Table 1 provides a representative suite of documented bombs and the analyses performed on each.

Polished thin sections of selected bombs were examined with backscatter electron (BSE) imaging and semi-quantitative Energy Dispersive X-Ray Spectroscopy (EDS) on the JEOL JXA-8260 Superprobe at

Victoria University of Wellington. Particle sizes on selected BSE images were measured using ImageJ (Schneider et al. 2012)~~ImageJ~~.

X-Ray computed tomography of ~~Bomb textures were examined in hand sample, thin sections, and with X-Ray computed tomography (CT) at two different scales (~13 and ~1.5 µm). L~~large samples (≤10 cm) ~~were~~ was performed~~scanned~~ in Hutch 3B of the Imaging and Medical Beamline at the Australian Synchrotron (Clayton), using their Ruby detector, 30 keV, and 0.8 s exposure time over 180° rotations, yielding reconstructed scans with voxel edge-lengths of ~13 µm. One bomb from this suite (P14-B02; Table 1, Fig. 3E) was then selected for high-resolution CT with the RX-Solutions Rescan at l'Université de Grenoble Alpes (France), after it was determined to be representative of Cordón Caulle composite bombs, and to contain the full spectrum of observed components within them (see Section 3)~~was selected for high-resolution CT with the RX-Solutions Rescan at l'Université de Grenoble Alpes (France)~~. This one~~e~~ bomb was sawn in half with a rock saw, and a small coring tool was used to extract 3 mm diameter cores from selected regions of interest. Each core was scanned using a LaB6 filament, 45 keV, 180° rotation, and 10 s exposure time, yielding reconstructed central subvolumes with voxel edge lengths of ~1.5 µm. Image stacks were manipulated using ImageJ ~~(Schneider et al. 2012)~~ and volumes rendered using Drishti Image (Limaye 2012). The Darcian permeabilities of selected CT subvolumes were modeled by Lattice Boltzmann simulation (Degruyter et al. 2010). Subvolumes for permeability simulation were 250x250x500 pixels, with flow simulated along the long direction. We used a low model inlet pressure (0.0005 MPa), and following Degruyter et al. (2010) we verified that an increase or decrease of this inlet pressure by more than two orders of magnitude did not result in any changes in modeled permeability, ensuring flow was in the low Reynolds (laminar) and Mach number regimes.

~~Polished thin sections of selected bombs were examined with backscatter electron (BSE) imaging and semi-quantitative Energy Dispersive X-Ray Spectroscopy (EDS) on the JEOL JXA-8260 Superprobe at Victoria University of Wellington.~~

3 Results

3.1 Bomb distributions and types

The "proximal" bomb field occupies a radial area <400 m from vent (Fig. 2A), and corresponds to the range of ballistic bomb deposition (impact and down-slope rolling/bouncing) observed during waning hybrid activity in January 2012 (Schipper et al. 2013). It is littered with countless blocks and bombs ranging from the decimetric scale to a maximum of ~2.5 metres across (Fig. 2B,D). The "distal" bomb field extends to up to 3.1 km from the vent, skewed toward the west/northwest (Fig. 2A). It is comprised of many bombs up to ~1 metre in size (although usually just remnant fragments of what were larger bombs), and are often associated with impact craters up to ~5 metres in diameter (Fig. 2C,E). The craters are several 10s of centimeters deep, and usually surrounded by a rim of pyroclastic debris that is coarser than the ash plain that they punctuate (Fig. 2E). Some craters cannot be linked to any specific bomb, indicating that the ballistics bounced, rolled, shattered, or were buried in the substrate they impacted (Fitzgerald et al. 2014).

Proximal bombs are the most texturally homogeneous of any observed at Cordón Caulle. Our fieldwork shows that most (~80 %) are angular, dense, and texturally similar to outer portions of the coherent lava flow. Their dull grey colour is similar to that of lava samples with >60% microlites in the groundmass (Schipper et al. 2019). They often have vesicles with a “frosted” appearance, similar to the vapour-phase cristobalite-bearing vesicles that are common in the lava flow (Schipper et al. 2015; Schipper et al. 2020) (Fig. 3A). The remaining (~20%) of proximal bombs are flow-banded and partially breadcrusted obsidian (Fig. 3B). Distal bombs (> 400 m to 3.1 km) are distinctly different. They are almost exclusively composites, or welded assemblages of many different particles (Fig. 3C-J). We refer to them as “composite bombs”, and note that they have been previously described as “spectacularly welded” bombs by Pistolesi et al. (2015), “pumice breccia” bombs by Castro et al. (2014), and “non-oxidized breccias” by Paisley et al. (2019b). Composite bombs are not apparent in our orthophotographs of the surface of the lava flow (Fig. 2B,D), although poor bomb/crater preservation would be expected on the lava itself (e.g., Fitzgerald et al. 2014). Our observations of composite bomb distribution are consistent with the stratigraphic reconstruction of Pistolesi et al. (2015) and observations of SERNAGEOMIN/OVDAS (2011) that link distal (composite) bomb emplacement to the high-energy ballistic phase of June 12-13 (Fig. ~~1E~~1D).

The lava-like proximal bombs do not show any sign of post-eruptive expansion or textural modification, and may be more accurately described as blocks (Fig. 3A). Partial expansion of proximal obsidian bombs is however apparent in preferential foaming along flow bands (Fig. 3B). Conversely, most composite bombs show evidence of having significantly expanded, or breadcrusted, after ejection. Some of the composite bombs have clear breadcrusting patterns on their surfaces (Fig. 3C), but in others the expansion is apparent in them being friable and having large and oxidized cavities in their interiors (Fig. 3D). The composite bombs appear to have breadcrusted *en masse*, such that at the time of ejection each bomb expanded as a single entity, with central cavities forming regardless of there being boundaries between the components within them.

The heterogeneity of the composite bombs is extreme. Over several field campaigns, the authors deliberated on how to best characterize them. Proposed types included “breadcrust bomb” (e.g., Fig. 3C), “pumice breccia” (e.g., Fig. 3D-F; Castro et al. 2014), “tuffisites” (Paisley et al. 2019a), “obsidian breccia” (e.g., Fig. 3G-H), “pebble bombs” or “honeycomb” (e.g., Fig. 3I; Whattam 2018), and “obsidian bombs with/without pumice” (e.g., Fig. 3J). Ultimately, these categories proved to have limited usefulness due to the large variability within them and gradational differences between them. Furthermore, field mapping showed no relationship between composite bomb type and distribution patterns. Here, we distil these categories into a unifying textural class of “composite” bombs: heterogeneity being their unifying characteristic.

3.2 Components of composite bombs

Composite bombs consist of assemblages of clasts with relatively homogenous internal textures and clear boundaries, bound together by borderless domains of matrix (Fig. 3D-H). The volume occupied by clasts is usually greater than that occupied by the matrix, with matrix often occupying sinuous inter-clast interstices (Fig. 3D-H). Rarely, clasts are relatively sparse and fully matrix-supported (Fig. 3I). In other rare bombs, no matrix is visible in hand sample; the composite nature of these pyroclasts is apparent in there being clasts of one texture fully embedded in larger domains of another (Fig. 3J). Individual composite bombs can look vastly different to each other, but are ultimately unified by being composite, each composed of a heterogeneous assemblage of clasts that are bound together by variable amounts of matrix material.

Clasts within composite bombs range from dense obsidian to highly vesicular pumice, with rare crystalline lithics. Even when a bomb is dominated by one type of clast, the presence of other types is common and striking (e.g., rare or minor obsidian within the pumice-dominated bombs of Fig. 3D-F, 4A-B). Further textural complexity is apparent within clasts when they are viewed in thin section (Fig. 4B) and BSE images (Fig. 4C-H).

Obsidian clasts range in size from few millimetres (Fig. 4B) to occupying almost the entirety of decimetric bombs and bomb fragments (Fig. 3J). Some obsidian is homogeneous, hypocrystalline rhyolitic glass (labeled "homogeneous obsidian" in Fig. 4C). Other obsidian has more complex microtextures in which unequivocal evidence for clastic origins ~~are~~ is preserved ("clastogenic obsidian" of Fig. 4C) (Castro et al. 2014). This evidence includes greyscale variations in BSE images that delineate where original (but now highly deformed) particle boundaries had been before densification (inset to Fig. 4C). It also includes the presence of mafic domains that are compositionally distinct to the dominant rhyolite, and could only have been incorporated as particles (Fig. 4C; see section 3.3). Individual obsidian clasts often contain regions that appear homogenous, and others that are obviously clastogenic (Fig. 4C,D).

Pumice clasts are white-to-beige, cover a similarly broad size range to the obsidian, and can be subdivided into two textural types. The first is "borderless" (sensu Saubin et al. 2016), with homogeneous textures throughout and no difference in vesicle texture from clast interiors to rims (Fig. 4E,H). Borderless pumices are usually flattened/deformed into angular-tipped fiamme. These tend to be aligned with adjacent pumice clasts to define a fabric similar to that in pumice-rich welded ignimbrites (Quane and Russell 2005; Wright and Cashman 2014) (e.g., inset to Fig. 3D, Fig. 4B). Other pumice clasts have large, extensively coalesced vesicles at their centres, but a radial gradation; first toward smaller, more isolated and increasingly flattened vesicles, and then to dense glassy margins (Fig. 4D-F). These are similar to the "pale vesicular clasts" with degassed borders that were described in tuffisites from Chaitén volcano (Saubin et al. 2016), and similar textures have been produced in experiments on expanding obsidian and shriveling pumice (Kennedy et al. 2016; von Aulock et al. 2017). We describe these as "foamed" pumice, as in most cases they appear to have isotropically expanded *in situ* within composite bombs (Fig. 4D,E). Although most of the foamed pumices are spheroidal, some are irregular in shape and have truncated vesicles that suggests they are no longer *in situ* (Fig. 4F). In particular, within matrix-dominated composite bombs (Fig. 3I) the foamed pumices have a flattened vesicular fabric that is oblique to the clast margins and these may have been rounded by abrasion in fluidized matrix material rather than foaming *in situ*.

The matrix is usually oxidized to brown or red in hand sample (Fig. 3D-I) and thin section (Fig. 4B). The degree of oxidation in Cordón Caulle pyroclastic material has previously been linked to the inverse depth of formation within the conduit (Paisley et al. 2019b), but here we note that oxidation also varies radially within ~~the~~ breadcrusted composite bombs (inset to Fig. 3D). In clast-dominated bombs, the matrix is in inter-clast tendrils that range in thickness from a few 10s of ~~micrometers~~ µm up to 10 mm (Fig. 3E-F, 4B). In BSE images, it is clear that the matrix is comprised of ash particles (Fig. 4D-H~~). The particles have an strong modal diameter of 10 - 20 µm, with only rare particles up to ~160 µm (Whattam 2018) and~~) that are preserved in various states of viscous sintering (Vasseur et al. 2013; Wadsworth et al. 2014) and compaction (Wadsworth et al. 2019) (Fig. 4D-H). Even within the area covered by a single thin section (Fig. 4B), matrix domains of similar sizes are preserved in vastly different states, from relatively porous (Fig. 4E) to almost completely dense (Fig. 4G). Furthermore, many high-porosity regions in the matrix have clearly foamed *in situ*. Similar to the foamed pumice clasts, these domains have dense margins but central cavities of large and extensively coalesced vesicles (Fig. 4H). Figure 5 shows the size distribution of 1525 ash particles, as measured on 61 BSE images from nine different composite bombs. The measured particles were mainly in matrix domains, but also included particles that were visible within clastogenic obsidian. Sintering particles have a strong modal diameter of 10 – 20 µm (45% of the counted particles), with rare particles up to ~175 µm.

3.3 Mafic component in composite bombs

There is compositional complexity in the Cordón Caulle composite bombs. Clastogenic domains (both clasts and matrix) contain a minor but pervasive mafic component (Fig. 4C-G). The mafic glass is basaltic andesite (55.6 – 62.1 wt% SiO_2) (Whattam 2018) that is brighter in BSE images than the low-silica rhyolitic glass~~e~~ (70.1 – 72.7 wt% SiO_2) that makes up the majority of the composite bombs, the pre-transition Plinian ejecta, and post-transition lava flow (Castro et al. 2013; Schipper et al. 2019). Mafic particles are usually in the ash size range (< 2 mm) but occasionally as big as small lapilli (Fig. 4B). Regardless of the local degree of sintering, boundaries between mafic and rhyolitic particles are sharp, and do not form compositionally mixed ~~continuums~~ continua along inter-particle necks (Fig. 4F,G). Mafic particles range from being glassy to having holocrystalline groundmass rich in quench microlites. Here, we simply use the presence of the mafic particles as a useful indicator of the clastogenic origin of any clast or domain in which they are hosted. Their presence reveals compositional complexity in the magmatic system that fed the 2011-2012 Cordón Caulle eruption, and their compositions, origins, and significance are currently being examined in a companion study.

3.4 X-Ray Computed Tomography and permeability modeling

Low-resolution (13 µm/voxel edge) CT scans provide an overview of the structure of composite bombs. In a low-density clast-dominated bomb, the irregular shapes and high-curvature or pointed tips of borderless pumice clasts are apparent (~~Fig. 5~~Fig. 6A). The matrix in this case is in relatively thin inter-clast domains that appear to suture neighbouring clasts together (~~Fig. 5~~Fig. 6A) (Gardner et al. 2017). In a rare but striking matrix-dominated bomb (Fig. 2I, and also Fig. 2b of Heap et al. 2019) banding of variable density is apparent in the matrix that wraps around the isolated pumice clasts (~~Fig. 5~~Fig. 6B). These are similar to the fine and coarse laminations observed in tuffisite veins within composite bombs described by Paisley et al. (2019a).

To investigate how sintering influenced open- and closed-system degassing, permeability modeling was performed on sub-volumes digitally extracted from high-resolution CT scans (~~Fig. 5~~Fig. 6C-D). The 1.5 µm/voxel edge resolution of these scans ensured that key permeability-controlling structures such as thin glass walls in vesicular regions and small interstitial pores in sintering regions were accounted for in the flow simulations. Four types of sub-volumes were digitally isolated. The first three captured singular textural domains: obsidian, pumice, or matrix. The fourth was a set of composite sub-volumes (e.g., ~~Fig. 5~~Fig. 6D) in which gas flow through variably textured domains was simulated (~~Fig. 5~~Fig. 6D-E). These were selected to investigate the effect of textural heterogeneity on porosity and permeability.

Obsidian clasts have porosity (ϕ) ranging from 0.07 to 0.17, and permeability (k) that spans three orders of magnitude, from $1\text{x}10^{-19}$ to $6.5\text{x}10^{-16}$ m^2. However, most of these have permeability < 10^{-18} m^2, with only one sample that had both the lowest porosity and highest permeability in the obsidian suite. Pumice clasts have porosity ranging from 0.66 to 0.75, and permeability ranging from $9.3\text{x}10^{-13}$ to $6.8\text{x}10^{-12}$ m^2. The matrix has intermediate porosity ranging from 0.20 to 0.58, and permeability from $1.4\text{x}10^{-14}$ to $2.1\text{x}10^{-12}$ m^2 (~~Fig. 5~~Fig. 6E).

A Kozeny-Carman type power-law best fit ($R^2 = 0.68$) to the matrix subvolumes is:

$$k = 8\text{x}10^{-12} \text{ x } \phi^{3.5} \qquad (1)$$

The fit to the matrix is strikingly similar to the scaled porosity-permeability relationship defined for sintering of volcanic ash with an initial particle diameter of 10 µm (Wadsworth et al. 2016), which is significant when recalling that the matrix formed by sintering of ash with a diameter of ~10-20 µm (Fig. 5). The best fit to the matrix extends to describe the porosity-permeability data from pumice clasts in the composite bombs, however all but one of obsidian clasts have dramatically lower permeability.

An example pumice-dominated sub-volume (Fig, 4D, example i) has porosity of 0.70 and permeability of $4.2\text{x}10^{-12}$ m^2, consistent with the data from pumice clasts. However, sub-volumes with more dramatic composite textures have permeabilities that are highly variable. In most cases they have lower permeability than matrix with equivalent porosity. This is most pronounced in the high-porosity composites ($\phi > 0.5$) where modeled permeabilities are up to two orders of magnitude lower than expected from the best fit to the modeled matrix (~~Fig. 5~~Fig. 6E). Many of the composite subvolumes fall within or below the porosity-permeability curves defined for fabric-parallel and –perpendicular multicomponent welded ignimbrites (Wright and Cashman 2014). Furthermore, the Wright and Cashman (2014) field encompasses only slightly higher permeability than that measured in a core extracted from a matrix-dominated Cordón Caulle composite bomb (Heap et al. 2019). The material measured by Heap et al. (2019) was extracted from the same matrix-dominated composite bomb shown in Figures 2I and 5B. We did not scan this bomb at high resolution and therefore cannot directly compare our modeled permeability with their measurements but note that such matrix-dominated bombs are relatively rare at Cordón Caulle.

Overall, the modeled porosity-permeability relationship for the matrix is consistent with the expected trend for viscous sintering of fine ash (Wadsworth et al. 2016). However, heterogeneous subvolumes of the Cordón Caulle composite bombs, which include multiple types of domains and interfaces between them are highly variable. They are more consistent with the porosity-permeability relationships observed in welded, multicomponent volcanic materials, especially at higher porosities (Wright and Cashman 2014; Heap et al. 2019).

4 Discussion

4.1 Composite bombs: clastogenic remnants of a conduit in transition

The high-energy ballistic emplacement of composite bombs bridged subplinian explosivity and lava flow emergence at Cordón Caulle (SERNAGEOMIN/OVDAS 2011; Castro et al. 2013; Pistolesi et al. 2015). The bombs themselves therefore represent the best available evidence of the textural state of magma in the shallow conduit when it was undergoing the explosive-effusive transition. Within the classical view that such transitions are controlled by a shift from closed- to open-system degassing (Eichelberger et al. 1986; Giachetti et al. 2020), magma in transitioning conduits might be expected to be high-permeability foams, or to be intensely crosscut by high-permeability fractures. Instead, the conduit was filled with a heterogeneous mixture of previously fragmented and variably welded/sintered clastic material, with permeability often much lower than expected for an equivalent magmatic porosity (~~Fig. 5~~Fig. 6E). This indicates that magmatic processes of textural evolution (e.g., vesiculating melt) played less of a deterministic role than clastogenic processes (e.g., fragmentation and sintering) in controlling outgassing, shifts in eruption style, and final textural evolution of eruptive products.

Magmatic processes describe a melt (± crystals) evolving by bubble nucleation, growth, and coalescence (Sparks 1978; Cashman and Mangan 1994). The fate of gas within the pore space is controlled by a hysteresis loop relative to percolation and permeability thresholds (Rust and Cashman 2004) that determine if the magma ultimately meets one of several criteria for fragmentation or outgases to be preserved as a coherent body of lava (e.g., Alidibirov and Dingwell 2000) (~~Fig. 6~~Fig. 7). It is increasingly recognized that clastogenic processes can also cause fragmented material to enter a qualitatively similar evolutionary path, albeit with significantly different threshold values (Tuffen et al. 2003; Tuffen and Dingwell 2005; Castro et al. 2012; Vasseur et al. 2013; Wadsworth et al. 2014; Wadsworth et al. 2016; Gardner et al. 2017; Gardner et al. 2018, 2019) (~~Fig. 6~~Fig. 7). Viscous sintering reduces porosity and permeability (Wadsworth et al. 2014; Kendrick et al. 2016; Wadsworth et al. 2016; Gardner et al. 2017), and increases strength (Kolzenburg et al. 2012; Vasseur et al. 2013). Sintering can ultimately yield a continuous melt (Gardner et al. 2018, 2019), and recent work even indicates that silicic lavas themselves may be generated in this way (Wadsworth et al. 2020). The most important difference between the magmatic and clastogenic evolutionary cycles is their percolation thresholds, which are an order of magnitude greater in vesiculating melts (ϕ ~0.3) than in sintering masses (ϕ ~0.03) (Wadsworth et al. 2016).

Magma rise in the Cordón Caulle conduit must have started with magmatic textural evolution as the rhyolite melt ascended from its 5-~~10~~ 9 km pre-eruptive storage zone (Castro et al. 2013; Delgado 2020), but clastogenic processes dominated textural evolution in the lead up to the explosive-effusive transition. The matrix in composite bombs is clearly a product of viscous sintering (Fig. 4E-G). Further, the clasts (lithics excepted) can be linked to different stages of clastogenic textural evolution (~~Fig. 6~~Fig. 7). Some obsidian is demonstrably clastogenic (inset to Fig. 4C), but “homogenous” obsidian (Fig. 4C) could equally be clastogenic but with evidence of the original particles having been completely erased. The absence of preserved particle outlines in “homogeneous” obsidian at Cordón Caulle is not necessarily evidence against it having had clastogenic origins. Here, it is noteworthy that residual water contents in pyroclastic obsidian at Cordón Caulle are very low (<0.3 wt.%; Schipper et al. 2013; Castro et al. 2014) compared to those found at other silicic volcanoes such as Mono Craters (≤ 2.71 wt.%; Newman et al. 1988) or Chaitén (≤ 1.6 wt.%Castro et al. 2014; Forte and Castro 2019). Although this is not in itself conclusive evidence that all Cordón Caulle obsidian is clastogenic, low residual H_2O would be expected if the obsidian clasts formed by sintering of shallowly-degassed fine ash. Furthermore, while the “borderless” pumice may represent portions of a magmatic foam, the “foamed” pumice (and matrix) appear to have expanded *in situ*. These pumices may also be clastogenic, with foaming having been driven by exsolution of residual H_2O from sintered melt, or by thermal expansion of H_2O that was entrapped between particles during the sintering process (Saubin et al. 2016; von Aulock et al. 2017; Forte and Castro 2019; Browning et al. 2020). Textures within the Cordón Caulle composite bombs demonstrate the importance of clastogenic textural evolution in a silicic conduit (~~Fig. 6~~Fig. 7), and highlight the vastly different textural states of melt that can be generated and closely juxtaposed within a transitioning conduit (Saubin et al. 2016; Isgett et al. 2017; Paisley et al. 2019b; Wadsworth et al. 2020).

Vulcanian eruptions often produce breccia bombs that demonstrate there to have been an abundance of fragmental material in the subsurface. The Cordón Caulle composite bombs are different from typical vent breccias (e.g., Yamagashi and Freebrey 1994) in that they have very low abundances of lithic/accidental clasts, and are instead comprised of juvenile products preserved in various states of viscous sintering~~(Yamagashi and Freebrey 1994)~~. Although some proportion of the composite bombs’ components may have accumulated by fallback into the vent, the assembly of these components into a composite mass was clearly driven by continuous delivery of fresh ash from below. The most striking evidence for this is the mafic component within the bombs’ clasts and matrix. No surface expression of mafic melts was documented during the 2011-2012 Cordón Caulle eruption, and no deposits of this compositionally distinct material have been found in our fieldwork. We conclude that the composite bombs represent material delivered directly from the subsurface to the shallow vent region, where it accumulated and sintered to various degrees.

4.2 No decline in fragmentation in the lead-up to effusion

The classical ~~traditional~~ equivalency drawn between fragmentation and explosivity ~~is continually under scrutiny~~has been challenged in recent times (e.g., Wadsworth et al. 2020). ~~In its traditional form, this argument implies~~ This traditional model posited that a decline in fragmentation efficiency – which is inversely proportional to the grainsize of the resulting particles (Kueppers et al. 2006) – should be expected in the lead-up to an explosive-effusive transition. If viewed macroscopically, the shift from ejection of sub-Plinian tephra to coarse composite bombs that occurred 8-9 days into the Cordón Caulle eruption (SERNAGEOMIN/OVDAS 2011; Castro et al. 2013; Pistolesi et al. 2015) marked a dramatic reduction in fragmentation efficiency. However, the particles that sintered to form the components of the composite bombs were originally of a very fine grainsize (~10 – 20 μm; Fig. 5) – finer than the modal grainsize of any deposits from the preceding explosive activity (Pistolesi et al. 2015; although direct comparison is difficult due to different tranport histories). The sizes of pyroclast upon ejection from a conduit are sometimes inversely linked to fragmentation depths (Dufek et al. 2012). Such a relationship can be logically envisioned for Cordón Caulle, with fine ash, clasts, and composite bombs representing the products of progressively shallower fragmentation events. U~~The u~~ltimately, the final fragmentation event that created the bombs may have been of low-efficiency, but the cycles of fragmentation that provided starting materials for sintering of their components were no less efficient than those that produced Plinian tephra. Furthermore, Cordón Caulle sustained an ash column throughout the ejection of composite bombs (Fig. 1E) and subsequent hybrid activity (Fig. 1F-G), indicating that some of the rising magma was being finely fragmented at all times during the eruption.

4.3 Timescales of in-conduit sintering

The small initial grainsize (~10 – 20 μm) of the in-conduit granular suspension would have been crucial to composite bomb formation and conduit closure. Sintering-driven matrix densification tracks with time (t) according to the characteristic sintering timescale in the absence of confining stresses (λ_S) (Vasseur et al. 2013; Wadsworth et al. 2014):

$$\phi(t) = \phi_i exp\left(-\frac{3t}{2\lambda_S}\right) \quad \text{with} \quad \lambda_S = \frac{\eta\bar{R}}{\sigma} \qquad (2)$$

where ϕ_i is the initial porosity (~0.45 for close –packed natural ash particles; Kendrick et al. 2016), and λ_S depends on particle radius (R), melt viscosity (η) and interfacial surface tension (σ = 0.22 Nm^{-1}). Viscosity is estimated to be 2.0x10^7 to 1.6x10^8 Pa s, using the model of Giordano et al. (2008) with an average pyroclast glass composition from Schipper et al. (2019), the 0.04 to 0.31 wt% range of H_2O measured in various composite bomb components by Castro et al. (2014), and a temperature of 900 ˚C. This is the upper end of the pre-eruptive storage temperature of the Cordón Caulle magma (Castro et al. 2013), but is justified by morphological inferences that the lava first emerged at ~900 ˚C (Magnall et al. 2017). This demonstrates that a high degree of thermal insulation in the conduit was maintained through the explosive-effusive transition, and suggests that the approach of lava-forming melt would have provided a significant source of heat to sintering materials entrapped in the upper conduit. The fine initial grainsize of the granular suspension at Cordón Caulle would also have ensured rapid diffusive hydration of sintering particles with hydration timescales (λ_D) similar to sintering timescales (λ_S) (calculated according to Gardner et al. 2018, 2019). Significant hydration of sintering materials is apparent in the foaming of bomb components (Fig. 4D,E,H) and the overall breadcrusting of composite bombs (Fig. 3C,D).

The time evolution of porosity (Eq. 2) and permeability (Eq. 1) indicate that only 13 (for H_2O = 0.31 wt%) to 109 (for H_2O = 0.04 wt%) minutes would be required for Cordón Caulle's subterranean granular suspension to drop below the percolation threshold (φ = 0.03; Wadsworth et al. 2016). Such rapid sintering timescales can explain why composite bombs can have juxtaposed materials of vastly different porosities and textures: the timescales of textural evolution are short enough that small local variations in H_2O, grainsize, or temperature could result in closely juxtaposed domains of clastogenic melt achieving very different positions in porosity-permeability space, even with evolutionary times that were only marginally different (Fig. 7). ~~Nearly identical~~Similarly short times (12 to 98 minutes) would be required for the permeability of the sintering matrix to drop below 10^{-16} m^2, a presumed cutoff between open- and closed-system degassing regimes (Collinson and Neuberg 2012). Although care must be taken in extrapolating from matrix permeabilities modeled at the micron-scale to inferences about full conduit closure, we note that matrix-bearing composite domains tend to have permeabilities that are significantly lower than expected for texturally homogeneous materials of equivalent porosity (Fig. 6E). This is presumably because (1) even thin tendrils of intercalated sintered matrix interfere with gas flow through the high-porosity ~~pumice~~clasts ~~domains~~, and (2) foamed pumice and matrix domains have poorly-vesicular margins that block gas flow (c.f., the closed foams of von Aulock et al. 2017). Therefore, the evolution of permeability within sintering matrix appears to have controlled the permeability evolution over longer lengthscales within the evolving Cordón Caulle conduit, but with ~~an~~the important caveat that~~:~~ our analyses do not capture the influence of large, interconnected pore spaces or pathways that may have existed in Cordón Caulle's shallow conduit. However, (1) the largest of observed pore spaces in Cordón Caulle composite bombs appear to be post-eruptive features; and (2) syn-eruptive observations indicated that preferential degassing pathways through the shallow conduit, although important, were relatively fixed in specific and discrete locations of shear localization within the conduit-plugging lava (Schipper et al. 2013).

Based on the observation that all components of the composite bombs were, or could have once been, finely fragmented material, we propose that the lead-up to the explosive-effusive transition at Cordón Caulle did not involve a reduction in fragmentation efficiency. Instead, maintained (or even increased) fragmentation efficiency yielded a subterranean granular suspension of very fine grainsize that rapidly sintered under hydrous conduit conditions, with commensurate reduction in porosity and permeability, and local resorption of H_2O to yield an impermeable and hydrous plug that was effective in choking off the main explosive phase of the eruption. Interestingly, although the production of fine ash required initial fragmentation to be efficient, the reduction in porosity that accompanies sintering of this material actually raises the amount of energy required to achieve fragmentation thresholds (Spieler et al. 2004). The diminution of tephra plumes at Cordón Caulle occurred because explosivity was "self-extinguishing", as efficient fragmentation actually enhanced the efficacy of sintering. It does not, however, represent a significant decline in fragmentation efficiency or energy.

4.4 Complex magma ascent in silicic fissures

Any vision of Cordón Caulle's plumbing system needs to accommodate several observed phenomena, including: (1) feeding of the initial Plinian eruption and subsequent changes in explosive character (Castro et al. 2013; Pistolesi et al. 2015); (2) accumulation of unerupted magma (of unconstrained coherence) in a sub-vent laccolith (Castro et al. 2016); (3) multiple, widely spaced deformation centres along the edifice (Jay et al. 2014; Delgado et al. 2016); (4) the recognition that the eruption tapped several similar-but-distinct melt bodies (Alloway et al. 2015); and (5) hybrid explosive-effusive activity (i.e., co-eruption of fragmented and coherent magma; Castro et al. 2013; Schipper et al. 2013). Furthermore, the composite bomb textures require a subsurface architecture that allowed: (1) efficient fragmentation of magma(s) into viscous rhyolite (+/- mafic) particles; (2) accumulation, viscous sintering and textural evolution into domains with textures represented by the clasts of composite bombs; (3) fracturing of these sintered materials to create pathways through and into which additional fine ash could transit and accumulate; and (4) accommodating transit of coherent~~, unfragmented~~ (or clastogenic; Wadsworth et al. 2020) lava-forming magma to the surface.

Such wide diversity of processes can be reconciled when remembering that Cordón Caulle is fed by a magmatic fissure system, in which there is significant magma movement laterally as well as vertically (Lara et al. 2006; Castro et al. 2013; Jay et al. 2014). The fissural character of Cordón Caulle was starkly expressed at the surface in the 1960 eruption, in which >20 vents opened along a 5.5 km long NW-SE fissure (Fig. 2A; Lara et al. 2004). Vents were comparatively focused in 2011-2012, but did show some rift-parallel shifts (Fig. 1G), and multiple loci of explosivity were maintained into the waning stages of hybrid activity (Schipper et al. 2013). Furthermore, in the first three days of the eruption, magma was fed from two distinct sources, 2-10 km along the fissure from the vent (Jay et al. 2014). Magma that rises in a structurally controlled fissure system can exploit pre-existing fractures/faults in accordance with local stress regimes (Lara et al. 2004) such that: (1) magma is not constrained to cylindrical conduit; (2) magma can exploit new paths of least resistance along strike of the fissure in the event of local blockage by sintering or other processes; and (3) magma that erupts explosively and effusively can have had entirely different ascent paths, instead of having to share a common path in which degassing regimes are required to change over time (Fig. 8~~7~~).

Ultimately, there was no apparent wholesale shift from processes causing explosivity to those causing effusivity at Cordón Caulle. Fragmentation continued throughout the eruption, but efficient sub-surface sintering eventually diminished its expression at the surface, in a process of "self-extinguishing". A clastic origin for silicic lava itself has been investigated in at Cordón Caulle (Castro et al. 2014), and has recently been argued for silicic lavas in general (Wadsworth et al. 2020). However, no textural evidence has been presented to show that the 2011-2012 lava flow itself has clastogenic origins (e.g., Schipper et al. (2019) found no evidence for mafic particles in their geochemical and textural investigation of ~20 samples from the 2011-2012 lava flow). This bears further investigation and the development of additional methods for examining cryptic and overprinted clastic signatures. However, based on available data, the 2011-2012 Cordón Caulle ~~Lava~~ lava does not appear to have resulted from a progressive decline in fragmentation efficiency, but the arrival of melt that evaded fragmentation – at least during its ultimate exit from the vent. In ~~the case of Cordón Caulle~~this case, the shift from explosive-to-effusive thus represents two distinctly separate, but overlapping, events: (1) the "self-extinguishing" of explosivity by viscous sintering, and (2) the arrival of coherent melt at the vent. The fact that these types of activity could occur simultaneously may at least partly be because Cordón Caulle's extensive fissure system provides a variety of magma ascent pathways in which decompression rates, shear, and other controls on eruptive style could vary (Taylor et al. 1983; e.g., Eichelberger et al. 1986; Newman et al. 1988; Degruyter et al. 2012; Nguyen et al. 2014; Cassidy et al. 2018). It is also important to note that continued fragmentation and sintering-driven conduit closure may have been the mechanism for the explosive-effusive transition at Cordón Caulle, but this does not preclude the transition having been driven or enhanced by extrinsic changes such as declining magma supply or ascent rates (Nguyen et al. 2014; Cassidy et al. 2018).

4.5 Equivalency of silicic conduits and tuffisite veins

Models of the plumbing system and shallow vent architecture at Cordón Caulle have evolved through a series of studies since the 2011-2012 eruption. Castro et al. (2013) described how magma delivery via a dike could have explained different ascent paths for explosively and effusively erupted magma. This interpretation remains valid, but the extent and complexity of magma recharge and withdrawal at Cordón Caulle was subsequently made clearer by analyses of edifice deformation (Jay et al. 2014; Delgado et al. 2016). Schipper et al. (2013) used observations of waning hybrid activity and textures of ash produced during the observed period and two bombs assumed to have been produced during Vulcanian blasts to describe Cordón Caulle's shallow vent as an outlet primarily choked by lava-forming magma that was crosscut by a branching network of permeable degassing structures that enabled gas fluxing from depth to be maintained. Their interpretations also remain valid, but lacking access to the full bomb field, they underestimated the degree to which the shallow conduit was filled with fragmented material rather than coherent melt. Paisley et al. (2019b) then presented a more complex vision of the Cordón Caulle conduit, including the recognition that repeated in-conduit fracturing was pervasive~~,~~ and important to producing the breccia bombs that were part of their analytical sample suite. Here, our new examination of composite bombs shows that subsurface, multi-generational fragmentation and sintering characterized the dynamics within the shallow conduit during the explosive-effusive transition at Cordón Caulle.

Clastic products dominated the conduit at Cordón Caulle in the days immediately preceding the emergence of lava (and have been recognized at other similar volcanoes; Adams et al. 2006), and permeability of this evolving composite material was controlled by viscous sintering. From a product perspective, there is significant textural similarity between clasts and matrix within the Cordón Caulle composite bombs and tuffisites from other volcanoes (e.g., Stasiuk et al. 1996; Tuffen and Dingwell 2005; Saubin et al. 2016). From a process perspective, tuffisite formation has been described as: (1) fragmentation and deposition of fragmental material; (2) sintering and magma backfilling; and (3) excavation and outgassing (Kendrick et al. 2016). The representative length scales over which these processes occur is the only fundamental difference between tuffisite veins and the conduit that was disrupted to produce the composite bombs at Cordón Caulle. Further, the recent study of Kolzenburg et al. (2019) treats edifice-penetrating tuffisite veins and pyroclast-filled conduits as fundamentally identical, although with different sizes and geometries. Their model showed rapid conductive cooling in tuffisites to lock-in high vein permeability, whereas slow cooling in cylindrical conduits creates a wide and efficient welding window that rapidly destroys original porosity, permeability, and outgassing potential. The Cordón Caulle composite bombs provide a robust example of this fundamental conduit-tuffisite equivalency.

5 Conclusions

We have investigated the textures of composite bombs ejected in the lead-up to the explosive-effusive transition at Cordón Caulle volcano (2011-2012). We find evidence that fine ash was continuously generated in the sub-surface throughout the eruption. The finely fragmented subterranean granular suspension was ideally suited to in-conduit viscous sintering that ultimately extinguished explosivity. Therefore, the appearance of lava at Cordón Caulle – and hence the onset of the explosive-effusive transition – may have depended more on rates of melt fracture and sintering, rather than on the generation of permeable outgassing pathways in a coherent, vesiculating melt body. We conclude that in order to accurately capture the controls on explosive-effusive transitions that are critical to mitigating the hazards from silicic eruptions, new models should incorporate clastogenic (sintering) processes of textural evolution into classical visions of magmatic textural evolution. Furthermore, we see silicic conduits and much-studied tuffisite veins to be phenomenologically identical, differing only in scale.

6 Acknowledgements

CIS acknowledges support from a Faculty Strategic Research Grant from VUW. BMK, RHF, ER, LNS and GS were supported by the Royal Society Te Apārangi Marsden project “Shaking magma to trigger volcanic eruptions”. RHF was additionally supported by a Ngāi Tahu Research Centre Doctoral Scholarship, Te Punenga Grant, and Mason Trust Grant. RP was supported by travel and research grants from McGill University. HT was supported by Royal Society University Research Fellowship UF140716. Acccess to the Australian Synchrotron was granted by ANSTO (M7045, M9095, M11725) and the New Zealand Synchrotron Group.

~~6~~7 References

Adams NK, Houghton BF, Fagents SA, Hildreth W (2006) The transition from explosive to effusive eruptive regime: The example of the 1912 Novarupta eruption, Alaska. Geol Soc Am Bull 118:620-634. doi:10.1130/B25768.1

Alidibirov M, Dingwell DB (2000) Three fragmentation mechanisms for highly viscous magma under rapid decompression. J Volcanol Geotherm Res 100:413-421.

Alloway BV, Pearce NJG, Villarosa G, Outes V, Moreno PI (2015) Multiple melt bodies fed the AD 2011 eruption of Puyehue-Cordón Caulle, Chile. Sci Reps 5:17589. doi:10.1038/srep17589

Browning J, Tuffen H, James MR, Owen J, Castro JM, Halliwell S, Wehbe K (2020) Post-fragmentation vesiculation timescales in hydrous rhyolitic bombs from Chaitén volcano. J S Am Earth Sci 104:102807. doi:10.1016/j.jsames.2020.102807

Cabrera A, Weinberg RF, Wright HMN (2015) Magma fracturing and degassing associated with obsidian formation: The explosive-effusive transition. J Volcanol Geotherm Res. doi:10.1016/j.jvolgeores.2014.12.014

Cabrera A, Weinberg RF, Wright HMN, Zlotnik S, Cas RAF (2011) Melt fracturing and healing: A mechanism for degassing of silicic obsidian. Geology 39:67-70. doi:10.1130/G31355.1

Cashman KV, Mangan MT (1994) Physical aspects of magmatic degassing; II, Constraints on vesiculation processes from textural studies of eruptive products. In: Carroll MR, et al. (eds) Volatiles in magmas, Reviews in Mineralogy, p^pp 447-478

Cashman KV, Sparks RSJ (2013) How volcanoes work: A 25 year perspective. Geol Soc Am Bull 125:643-663. doi:10.1130/B30720.1

Cassidy M, Manga M, Cashman KV, Bachmann O (2018) Controls on explosive-effusive volcanic eruption styles. Nature Comms 9:2893. doi:10.1038/s41467-018-05293-3

Castro JM, Bindeman IN, Tuffen H, Schipper CI (2014) Explosive origin of silicic lava: Textural and δD-H2O evidence for pyroclastic degassing during rhyolite effusion. Earth Planet Sci Lett 405:52-61. doi:10.1016/j.epsl.2014.08.012

Castro JM, Cordonnier B, Schipper CI, Tuffen H, Baumann T, Feisel Y (2016) Rapid laccolith intrusion driven by explosive volcanic eruption. Nature Comms 7:13585. doi:10.1038/ncomms13585

Castro JM, Cordonnier B, Tuffen H, Tobin MJ, Puskar L, Martin MC, Bechtel HA (2012) The role of melt-fracture degassing in defusing explosive rhyolite eruptions at volcán Chaitén. Earth Planet Sci Lett 333-334:63-69. doi:10.1016/j.epsl.2012.04.024

Castro JM, Gardner JE (2008) Did magma ascent rate control the explosive-effusive tranisiton at the Inyo volcanic chain, California? Geology 36:279-282. doi:10.1130/G24453A.1

Castro JM, Schipper CI, Amigo A, Silva Parejas C, Mueller S, Jacob D, Militzer AS (2013) Storage and eruption of near-liquidus rhyolite magma at Cordón Caulle, Chile. Bull Volcanol 75:702. doi:10.1007/s00445-013-0702-9

Collinson ASD, Neuberg JW (2012) Gas storage, transport and pressure changes in an evolving permeable volcanic edifice. J Volcanol Geotherm Res 243-244:1-13. doi:10.1016/j.jvolgeores.2012.06.027

Degruyter W, Bachmann O, Burgisser A, Manga M (2012) The effects of outgassing on the transition between effusive and explosive silicic eruptions. Earth Planet Sci Lett 349-350:161-170.

Degruyter W, Burgisser A, Bachmann O, Malaspinas O (2010) Synchotron X-ray microtomography and lattice Boltzmann simulations of gas flow through volcanic pumices. Geosphere 6:470-481. doi:10.1130/GES00555.1

Delgado F (2020) Rhyolitic volcano dynamics in the Southern Andes: Contributions from 17 years of InSAR observations at Cordón Caulle from 2003 to 2020. J S Am Earth Sci 102841. doi:10.1016/j.jsames.2020.102841

Delgado F, Pritchard ME, Basualto D, Lazo J, Córdova L, Lara LE (2016) Rapid reinflation following the 2011– 2012 rhyodacite eruption at Cordón Caulle volcano (Southern Andes) imaged by InSAR: Evidence for magma reservoir refill. Geophys Res Lett 43:9552-9562. doi:10.1002/ 2016GL070066

Delle Donna D, Harris AJL, Ripepe M, Wright R (2010) Earthquake-induced thermal anomalies at active volcanoes. Geology 38:771-774. doi:10.1130/G30984.1

Dufek J, Manga M, Patel A (2012) Granular disruption during explosive volcanic eruptions. Nature Geosci 5:561-564. doi:10.1038/NGEO1524

Eichelberger JC (1995) Silicic Volcanism: Ascent of viscous magmas from crustal reservoirs. Annu Rev Earth Planet Sci 23:41-63.

Eichelberger JC, Carrigan CR, Westrich HR, Price RH (1986) Non-explosive silicic volcanism. Nature 323:598-602. doi:10.1038/323598a0

Eichelberger JC, Westrich HR (1981) Magmatic volatiles in explosive rhyolitic eruptions. Geophys Res Lett 8:757-760. doi:10.1029/GL008i007p00757

Elissondo M, Baumann V, Bonadonna C, Pistolesi M, Cioni R, Bertagnini A, Biass S, Herrero J-C, Gonzales R (2016) Chronology and impact of the 2011 Cordón Caulle eruption, Chile. Nat Hazards Earth Syst Sci 16:675-704. doi:10.5194/nhess-16-675-2016

Farquharson JI, Wadsworth FB, Heap MJ, Baud P (2017) Time-dependent permeability evolution in compacting volcanic fracture systems and implications for gas overpressure. J Volcanol Geotherm Res 339:81-97. doi:10.1016/j.jvolgeores.2017.04.025

Fitzgerald RH, Tsunematsu K, Kennedy BM, Breard ECP, Lube G, Wilson TM, Jolly AD, Pawson J, Rosenberg MD, Cronin SJ (2014) The application of a calibrated 3D ballistic trajectory model to ballistic hazard assessments at Upper Te Maari, Tongariro. J Volcanol Geotherm Res 286:248-262. doi:10.1016/j.jvolgeores.2014.04.006

Forte P, Castro JM (2019) H_2O-content and temperature limit the explosive potential of rhyolite magma during Plinian eruptions. Earth Planet Sci Lett 506:157-167. doi:10.1016/j.epsl.2018.10.041

Gardner JE, Llewellin EW, Watkins JM, Befus KS (2017) Formation of obsidian pyroclasts by sintering of ash particles in the volcanic conduit. Earth Planet Sci Lett 459:252-263. doi:10.1016/j.epsl.2016.11.037

Gardner JE, Wadsworth FB, Llewellin EW, Watkins JM, Coumans JP (2018) Experimental sintering of ash at conduit conditions and implications for the longevity of tuffisites. Bull Volcanol 80:23. doi:10.1007/s00445-018-1202-8

Gardner JE, Wadsworth FB, Llewellin EW, Watkins JM, Coumans JP (2019) Experimental constraints on the textures and origin of obsidian pyroclasts. Bull Voclanol 81:12. doi:10.1007/s00445-019-1283-z

Gerlach DC, Frey FA, Moreno-Roa H, Lopez-Escobar L (1988) Recent volcanism in the Puyehue-Cordón Caulle region, southern Andes, Chile (40.5o S): Petrogenesis of evolved lavas. J Petrol 29:333-382.

Giachetti T, Hudak MR, Shea T, Bindeman IN, Hoxsie EC (2020) D/H ratios and H_2O contents record degassing and rehydration history of rhyolitic magma and pyroclasts. Earth Planet Sci Lett 530:115909. doi:10.1016/j.epsl.2019.115909

Giordano D, Russell JK, Dingwell DB (2008) Viscosity of magmatic liquids: A model. Earth Planet Sci Lett 271:123-134. doi:10.1016/j.epsl.2008.03.038

Gonnermann HM, Manga M (2003) Explosive volcanism may not be an inevitable consequence of magma fragmentation. Nature 426:432-435.

Heap MJ, Tuffen H, Wadsworth FB, Reuschlé T, Castro JM, Schipper CI (2019) The permeability evolution of tuffisites and implications for outgassing through dense rhyolitic magma. J Geophys Res Solid Earth 124:8281-8299. doi:10.1029/2018JB017035

Isgett SJ, Houghton BF, Fagents SA, Biass S, Burgisser A, Arbaret L (2017) Eruptive and shallow conduit dynamics during Vulcanian explosions: insights from the Episode IV block field of the 1912 eruption of Novarupta, Alaska. Bull Volcanol 79:58. doi:10.1007/s00445-017-1138-4

Jay J, Costa F, Pritchard M, Lara LE, Singer BS, Herrin J (2014) Locating magma reservoirs using InSAR and petrology before and during the 2011-2012 Cordón Caulle silicic eruption. Earth Planet Sci Lett 395:254-266. doi:10.1016/j.epsl.2014.03.046

Kendrick JE, Lavallée Y, Varley N, Wadsworth FB, Lamb OD, Vasseur J (2016) Blowing Off Steam: Tuffisite Formation As a Regulator for Lava Dome Eruptions. Front Earth Sci 4:41. doi:10.3389/feart.2016.00041

Kennedy BM, Wadsworth FB, Vasseur J, Schipper CI, Jellinek AM, von Aulock FW, Hess K-U, Russell JK, Lavallée Y, Nichols ARL, Dingwell DB (2016) Surface tension driven processes densify and retain permeability in magma and lava. Earth Planet Sci Lett 433:116-124. doi:10.1016/j.epsl.2015.10.031

Kolzenburg S, Heap MJ, Lavallée Y, Russell JK, Meredith PG, Dingwell DB (2012) Strength and permeability recovery of tuffisite-bearing andesites. Solid Earth 3:191-198. doi:10.5194/se-3-191-2012

Kolzenburg S, Ryan AG, Russell JK (2019) Permeability evolution during non-isothermal compaction in volcanic conduits and tuffisite veins: Implications for pressure monitoring of volcanic edifices. Earth Planet Sci Lett 527:115783. doi:10.1016/j.epsl.2019.115783

Kueppers U, Scheu B, Spieler O, Dingwell DB (2006) Fragmentation efficiency of explosive volcanic eruption: A study of experimentally generated pyroclasts. J Volcanol Geotherm Res 153:125-135. doi:10.1016/j.jvolgeores.2005.08.006

Lara LE (2008) The 2008 eruption of the Chaitén Volcano, Chile: a preliminary report. Andean Geol 36:125-129.

Lara LE, Moreno H, Naranjo JA, Matthews S, Pérez de Arce C (2006) Magmatic evolution of the Puyehue-Cordón Caulle Volcanic Complex (40˚ S), Southern Andean Volcanic Zone: From shield to unusual rhyolite fissure volcanism. J Volcanol Geotherm Res 157:343-366.

Lara LE, Naranjo JA, Moreno H (2004) Rhyodacitic fissure eruption in Southern Andes (Cordón Caulle; 40.5˚S) after the 1960 (Mw: 9.5) Chilean earthquake: A structural interpretation. J Volcanol Geotherm Res 138:127-138.

Limaye A (2012) Drishti: a volume exploration and presentation tool. In: Developments in X-Ray Tomography VIII.

Magnall N, James MR, Tuffen H, Vye-Brown C (2017) Emplacing a cooling-limited rhyolite lava flow: Similarities with basaltic lava flows. Front Earth Sci 5:44. doi:10.3389/feart.2017.00044

Newman S, Epstein S, Stolper EM (1988) Water, carbon dioxide, and hydrogen isotopes in glasses from the ca. 1340 A.D. eruption of the Mono Craters, California: Constraints on degassing phenomena and initial volatile content. J Volcanol Geotherm Res 35:75-96.

Nguyen CT, Gonnermann HM, Houghton BF (2014) Explosive to effusive transition during the largest volcanic eruption of the 20th century. Geology 42:703-706. doi:10.1130/G35593.1

Paisley R, Berlo K, Ghaleb B, Tuffen H (2019a) Geochemical constraints on the role of tuffisite veins in degassing at the 2008-09 Chaitén and 2011-12 Cordón Caulle rhyolite eruptions. J Volcanol Geotherm Res 380:80-93. doi:j.jvolgeores.2019.05.013

Paisley R, Berlo K, Whattam J, Schipper CI, Tuffen H (2019b) Degassing-induced chemical heterogeneity at the 2011-2012 Cordón Caulle eruption. Volcanica 2:211-237. doi:10.30909/vol.02.02.211237

Pallister JS, Diefenbach AK, Burton WC, Muñoz J, Griswold JP, Lara LE, Lowenstern JB, Valenzuela CE (2013) The Chaitén rhyolite lava dome - Eruption sequence, lava dome volumes, rapid effusion rates and source of the rhyolite magma. Andean Geology 40:277-294. doi:10.5027/andgeoV40n2-a0?6?

Pistolesi M, Cioni R, Bonadonna C, Elissondo M, Baumann V, Bertagnini A, Chiari L, Gonzales R, Rosi M, RFrancalanci L (2015) Complex dynamics of small-moderate volcanic events: the example of the 2011-12 rhyolitic Cordón Caulle eruption, Chile. Bull Volcanol 77:3. doi:10.1007/s00445-014-0898-3

Quane SL, Russell JK (2005) Ranking welding intensity in pyroclastic deposits. Bull Voclanol 67:129-143. doi:10.1007/s00445-004-0367-5

Rust AC, Cashman KV (2004) Permeability of vesicular silicic magma: inertial and hysteresis effects. Earth Planet Sci Lett 228:93-107. doi:10.1016/j.epsl.2004.09.025

Rust AC, Cashman KV, Wallace P (2004) Magma degassing buffered by vapour flow through brecciated conduit margins. Geology 32(4):349-352.

Saubin E, Tuffen H, Gurioli L, Owen J, Castro JM, Berlo K, McGowan E, Schipper CI, Wehbe K (2016) Conduit dynamics in transitional rhyolitic activity recorded by tuffisite vein textures from the 2008-2009 Chaitén eruption. Frontiers Earth Sci Volcanol 4:59. doi:10.3389/feart.2016.00059

Sawi TM, Manga M (2018) Revisiting short-term earthquake triggered volcanism. Bull Volcanol 80:57. doi:10.1007/s00445-018-1232-2

Schipper CI, Castro JM, Kennedy BM, Christenson BW, Aiuppa A, Alloway BV, Forte P, Seropian G, Tuffen H (2019) Halogen (Cl, F) and sulphur release during explosive, effusive, and intrusive phases of the 2011 rhyolitic eruption at Cordón Caulle volcano (Chile). Volcanica 2:73-90. doi:10.30909/vol.02.01.7390

Schipper CI, Castro JM, Tuffen H, James MR, How P (2013) Shallow vent architecture during hybrid explosive-effusive activity at Cordón Caulle (Chile, 2011-12): Evidence from direct observations and pyroclast textures. J Volcanol Geotherm Res 262:25-37. doi:10.1016/j.jvolgeores.2013.06.005

Schipper CI, Castro JM, Tuffen H, Wadsworth FB, Chappell D, Pantoja AE, Simpson M, Le Ru EC (2015) Cristobalite in the 2011-12 Cordón Caulle eruption (Chile). Bull Volcanol 77:34. doi:10.1007/s00445-015-0925-z

Schipper CI, Rickard WDA, Reddy SM, Saxey DW, Castro JM, Fougerouse D, Quadir Z, Conway CE, Prior DJ, Lilly K (2020) Volcanic SiO_2-Cristobalite: A natural product of chemical vapor deposition. Amer Mineral 105:510-524. doi:10.2138/am-2019-7236

Schneider CA, Rasband WS, Eliceiri KW (2012) NIH Image to ImageJ: 25 years of image analysis. Nature Methods 9:671-675.

SERNAGEOMIN/OVDAS (2011) 38.

Silva Parejas C, Lara LE, Bertin D, Amigo A, Orozco G (2012) The 2011-2012 eruption of Cordón Caulle volcano (Southern Andes): Evolution, crisis management and current hazards. EGU General Assembly Abstracts 14(EGU2012-9382-2).

Sparks RSJ (1978) The dynamics of bubble formation and growth in magmas: A review and analysis. J Volcanol Geotherm Res 3:1-37.

Spieler O, Kennedy B, Kueppers U, Dingwell DB, Scheu B, Taddeucci J (2004) The fragmentation threshold of pyroclastic rocks. Earth Planet Sci Lett 226:139-148.

Stasiuk MV, Barclay J, Carroll MR, Jaupart C, Ratté JC, Sparks RSJ, Tait SR (1996) Degassing during magma ascent in the mule creek vent (USA). Bull Volcanol 58:117-130.

Taylor BE, Eichelberger JC, Westrich HR (1983) Hydrogen isotopic evidence of rhyolitic magma degassing during shallow intrusion and eruption. Nature 306:541-545. doi:10.1038/306541a0

Tuffen H, Dingwell D (2005) Fault textures in volcanic conduits: Evidence for seismic trigger mechanisms during silicic eruptions. Bull Volcanol 67:370-387. doi:10.1007/s00445-004-0383-5

Tuffen H, Dingwell DB, Pinkerton H (2003) Repeated fracturing and healing of silicic magma generate flow banding and earthquakes? Geology 31:1089-1092.

Tuffen H, James MR, Castro JM, Schipper CI (2013) Exceptional mobility of an advancing rhyolitic obsidian flow at Cordón Caulle volcano in Chile. Nature Comm 4:2709. doi:10.1038/ncomms3709

Tuffen H, Smith R, Sammonds PR (2008) Evidence for seismogenic fracture of silicic magma. Nature 453:511-514. doi:10.1038/nature06989

Vasseur J, Wadsworth FB, Lavallée Y, Hess K-U, Dingwell DB (2013) Volcanic sintering: Timescales of viscous densification and strength recovery. Geophys Res Lett 40:5658-5664. doi:10.1002/2013GL058105

von Aulock FW, Kennedy BM, Maksimenko A, Wadsworth FB, Lavallée Y (2017) Outgassing from open and closed magma foams. Frontiers Earth Sci Volcanol 5:46. doi:10.3389/feart.2017.00046

Wadsworth FB, Llewellin EW, Vasseur J, Gardner JE, Tuffen H (2020) Explosive-effusive volcanic eruption transitions caused by sintering. Sci Adv 6:eaba7940. doi:10.1126/sciadv.aba7940

Wadsworth FB, Vasseur J, Schauroth J, Llewellin EW, Dobson KJ, Havard T, Scheu B, von Aulock FW, Gardner JE, Dingwell DB, Hess K-U, Colombier M, Marone F, Tuffen H, Heap MJ (2019) A general model for welding of ash particles in volcanic systems validated using *in situ* X-ray tomography. Earth Planet Sci Lett 525:115726. doi:10.1016/j.epsl.2019.115726

Wadsworth FB, Vasseur J, Scheu B, Kendrick JE, Lavallée Y, Dingwell DB (2016) Universal scaling of fluid permeability during volcanic welding and sediment diagenesis. Geology 44:219-222. doi:10.1130/G37559.1

Wadsworth FB, Vasseur J, von Aulock FW, Hess K-U, Scheu B, Lavallée Y, Dingwell DB (2014) Nonisothermal viscous sintering of volcanic ash. J Geophys Res 119:8792-8804. doi:10.1002/2014JB011453

Wang C, Luo ZJ, Huang X (2011) Parallax correction in collocating CloudSat and Moderate Resolution Imaging Spectroradiometer (MODIS) observations: Method and application to convection study. J Geophys Res 116:D17201. doi:10.1029/2011JD016097

Whattam J (2018) Under the surface: Textural analysis of complex, multi-component Vulcanian bombs produced during the hybrid explosive-effusive phase of the 2011-2012 Cordón Caulle eruption, Chile. MSc thesis. Victoria University of Wellington, Wellington, p 152

Wright HMN, Cashman KV (2014) Compaction and gas loss in welded pyroclastic deposits as revealed by porosity, permeability, and electrical conductivity measurements of the Shevlin Park Tuff. Geol Soc Am Bull 126:234-247. doi:10.1130/B30668.1

Yamagashi H, Freebrey C (1994) Ballistic ejecta from the 1988-1989 andesitic Vulcanian eruptions of Tokachidake volcano, Hapan: morphological features and genesis. J Volcanol Geotherm Res 59:269-278. doi:10.1016/0377-0273(94)90082-5

Figure Captions

Figure 1. Location and eruption progression. **A-F**. Terra/MODIS (NASA Worldview) images spanning the first 16 days of the 2011-2012 Cordón Caulle eruption. Apparent shift in vent location from June 5 – 7 is a function of different off-nadir view angles; once corrected for parallax the vent locations are within error of each other (Wang et al. 2011). Deformation centres identified in INSAR interferograms by Jay et al. (2014). ~~Inset to F shows location of the Puyehue-Cordón Caulle Volcanic Complex (PCVCC).~~ **G**. GeoEye-1 image of multiple vents, ~2 weeks after lava emergence. Inset shows location of the Puyehue-Cordón Caulle Volcanic Complex (PCVCC).

Figure 2. Bomb distributions. **A**. Recent deposits from Cordón Caulle (Google Earth Image taken 4 Oct, 2012 by Maxar Technologies, 2020). Red points are sampled composite bombs, dashed lines mark approximate extents of "proximal" and "distal" bomb fields. Boxes show locations of images in B-C. **B-C**. Orthographic images from a 2017 overflight of Cordón Caulle (Schipper et al., unpublished data). **B**. The 2011-2012 vent(s), littered with dark, dense, proximal lava bombs that lack ballistic impact craters. **C**. An ash-covered topographic high that is heavily pockmarked by ballistic impact craters. **D-E**. Photographs of proximal bomb field (D) and typical impact crater in distal bomb field (E).

Figure 3. Cordón Caulle bombs. **A**. Proximal lava bombs/blocks. **B**. Proximal obsidian bomb with localized expansion along some flow bands. **C-D**. Breadcrusted composite bombs. Inset to (D) shows cavity at the bomb's centre indicating *en masse* expansion regardless of multicomponent structure. **E-F**. Low-density composite bombs primarily composed of flattened pumice in an oxidized matrix. The bombs shown in (E) was selected for high-resolution CT analysis. **G-H**. High-density composite bombs. Similar in overall structure to (D-F), but with a higher proportion of dense clasts. **I**. Composite bomb in which matrix volumetrically dominates over clasts. **J**. Obsidian bomb lacking any obvious matrix, but still composite due to containing pumice clasts.

Figure 4. Textures of composite bombs. **A**. Breadcrusted composite bomb from which all images were collected. **B**. Flatbed scan of thin section. Large brown vesicular clast in the centre is mafic. **C-H**. BSE images from the thin section in (B). Red arrows indicate some of the mafic particles, which appear lighter than rhyolite in BSE images. Orange dashed lines indicate boundaries between domains where identifiable. **C**. Obsidian with "homogeneous" region and "clastogenic" region that contains mafic domains and particle outlines that reveal a clastic origin. Interface is expanded in inset frame. **D**. Pumices that have isotropically foamed *in situ*, bound to obsidian and other clasts by sintered matrix. **E**. Thick matrix domain separating borderless and foamed pumice clasts. Note that the matrix maintains significant porosity despite constituent particles being flattened parallel to the long axis of the domain itself. **F**. Two foamed pumice clasts bound by mafic-bearing matrix material. Note that vesicles in the right-hand pumice are flattened against the matrix domain. **G.** Low-porosity matrix. Most of the pore space is adjacent to mafic particles. **H**. Matrix that has vesiculated *in situ* after binding together crystalline lithic and borderless pumice clasts. The matrix shown in E-H roughly delineate a progression in textural evolution, first on a sintering path of declining porosity from E to G, and then a path of vesiculation from G to H.

Figure 5. Histogram of particle sizes (5 µm bins) within sintering and/or clastogenic domains. 2D Particle diameters (n = 1525) were measured on 61 BSE images from nine different composite bombs. The measured particles are dominantly from within matrix domains, but identifiable particles from within clastogenic obsidian were also included in the count where possible (e.g., mafic particles in Fig. 4B). The size range of 10 – 20 µm accounts for 45% of particles.

Figure 6~~5~~. CT investigation of composite bombs. **A-B**. 3D renderings of low-resolution CT scans of clast-dominated (A) and matrix-dominated (B) composite bombs. **C**. High-resolution 3D rendering of composite bomb material, capturing a wide range of different components. **D**. Example subvolumes isolated from (C), upon which Lattice Boltzmann permeability simulations were performed. Lower case Roman numerals link these specific volumes to their porosities and permeabilities in (E) **E**. Porosity-permeability plot for composite bomb components, against relationships for sintering of monodisperse rhyolite particles (Wadsworth et al. 2016) and natural welded tuffs (Wright and Cashman 2014).

Figure ~~6~~7. A qualitative magmatic-clastogenic textural evolution cycle in porosity (φ) – permeability (k) space. Figure is based on the ~~porosity-permeability~~ hysteresis loop described by (Rust and Cashman 2004) and illustrated by (Cashman and Sparks 2013). Processes are marked within axes, and products are indicated outside axes. The magmatic and clastogenic cycles begin (at t_o) from a coherent bubble-free melt and a fragmented granular suspension, respectively. The colours of arrows and text indicate which processes and products are unique to each cycle or common to both. Note that all textures observed in Cordón Caulle composite bombs can be achieved by clastogenic processes, but not all can be linked to magmatic processes. The figure is necessarily qualitative because key limits such as the percolation threshold (ϕ_c) are vastly different in magmatic ($0.2 \leq \phi_c \leq 0.7$) and clastogenic ($\phi_c \approx 0.03$) systems (Wadsworth et al. 2016 and references therein).

Figure 8~~Figure 7~~. Schematic portrayal of the evolution of clastogenic processes in the first 10 days of the 2011-2012 Cordón Caulle eruption. Images are roughly to scale in the horizontal, based on the surface expressions of the laccolith and vent (e.g., as in Fig. 2A). Vertical is not to scale.

Fig.1

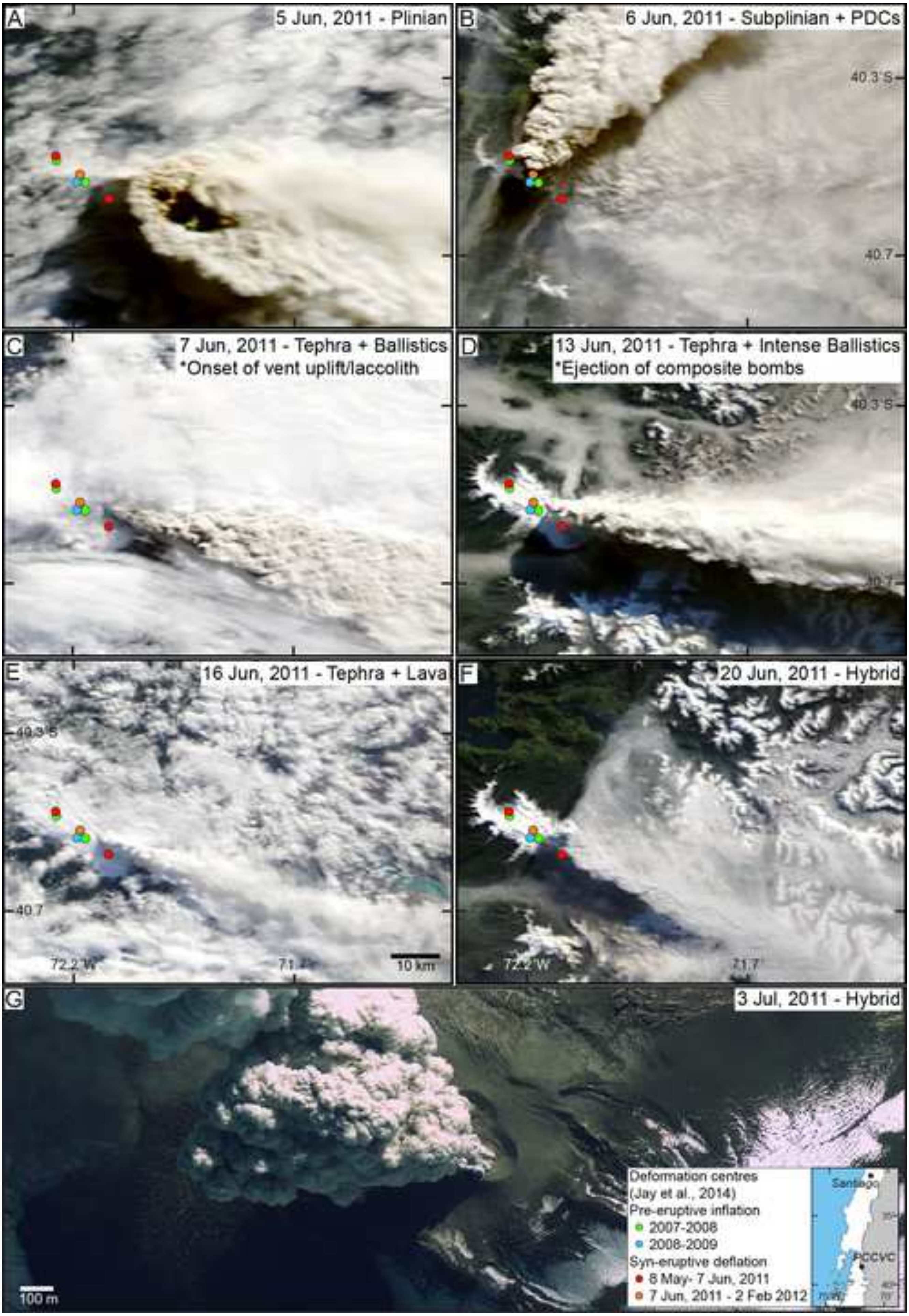

A
5 Jun, 2011 - Plinian
B
6 Jun, 2011 - Subplinian + PDCs
40.3°S
40.7
C
7 Jun, 2011 - Tephra + Ballistics
*Onset of vent uplift/laccolith
D
13 Jun, 2011 - Tephra + Intense Ballistics
*Ejection of composite bombs
40.3°S
40.7
E
16 Jun, 2011 - Tephra + Lava
40.3°S
40.7
72.2°W
71.7
10 km
F
20 Jun, 2011 - Hybrid
72.2°W
71.7
G
3 Jul, 2011 - Hybrid
100 m
Deformation centres
(Jay et al., 2014)
Pre-eruptive inflation
2007-2008
2008-2009
Syn-eruptive deflation
8 May- 7 Jun, 2011
7 Jun, 2011 - 2 Feb 2012
Santiago
PCCVC

Fig.2

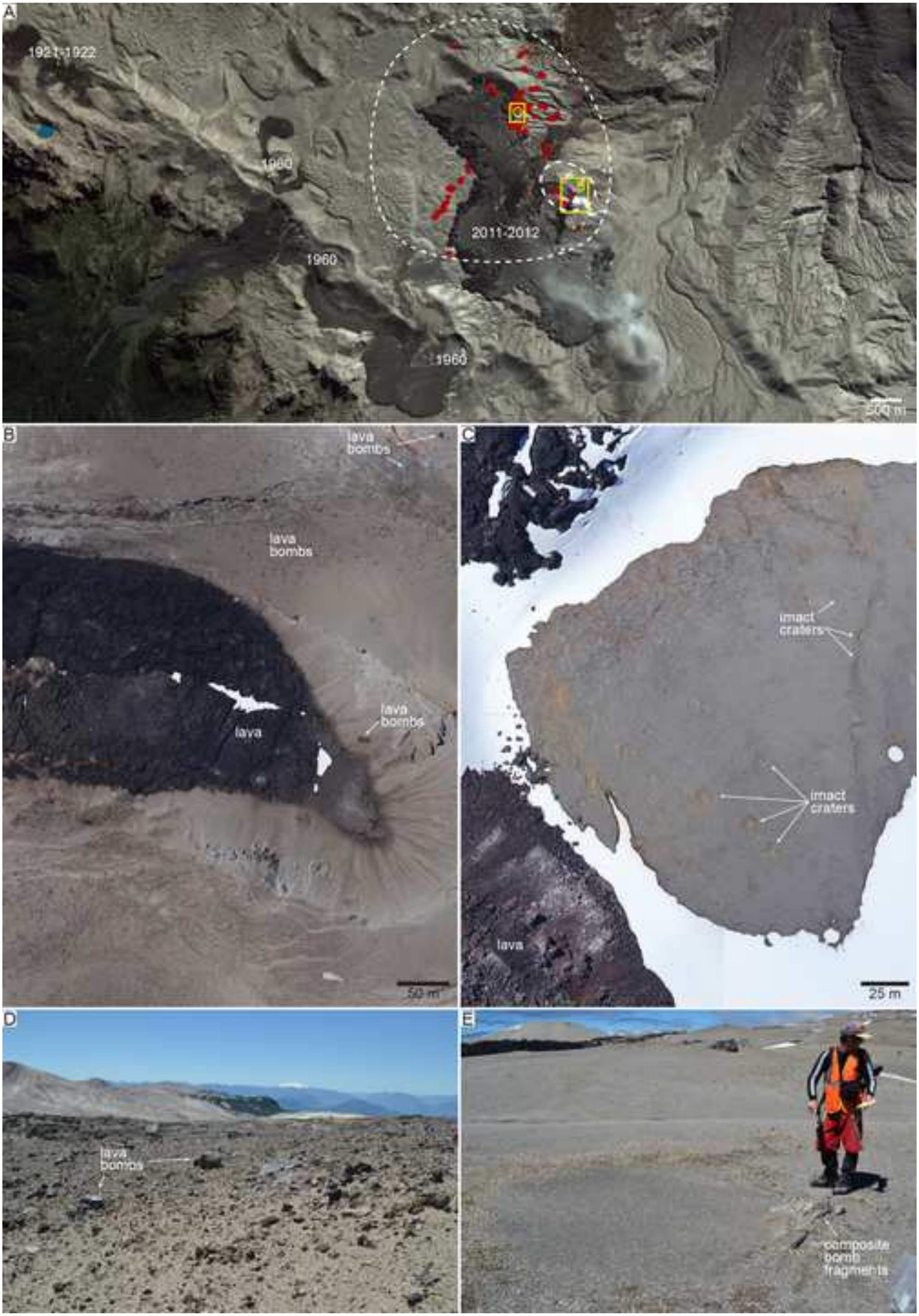
A
1921-1922
1960
1960
1960
2011-2012
500 m
B
lava bombs
lava bombs
lava bombs
lava
50 m
C
imact craters
imact craters
lava
25 m
D
lava bombs
E
composite bomb fragments

Fig.3


Proximal Homogeneous Bombs
A
B
Distal Composite Bombs
C
D
E
F
G
H
I
J

Fig.4

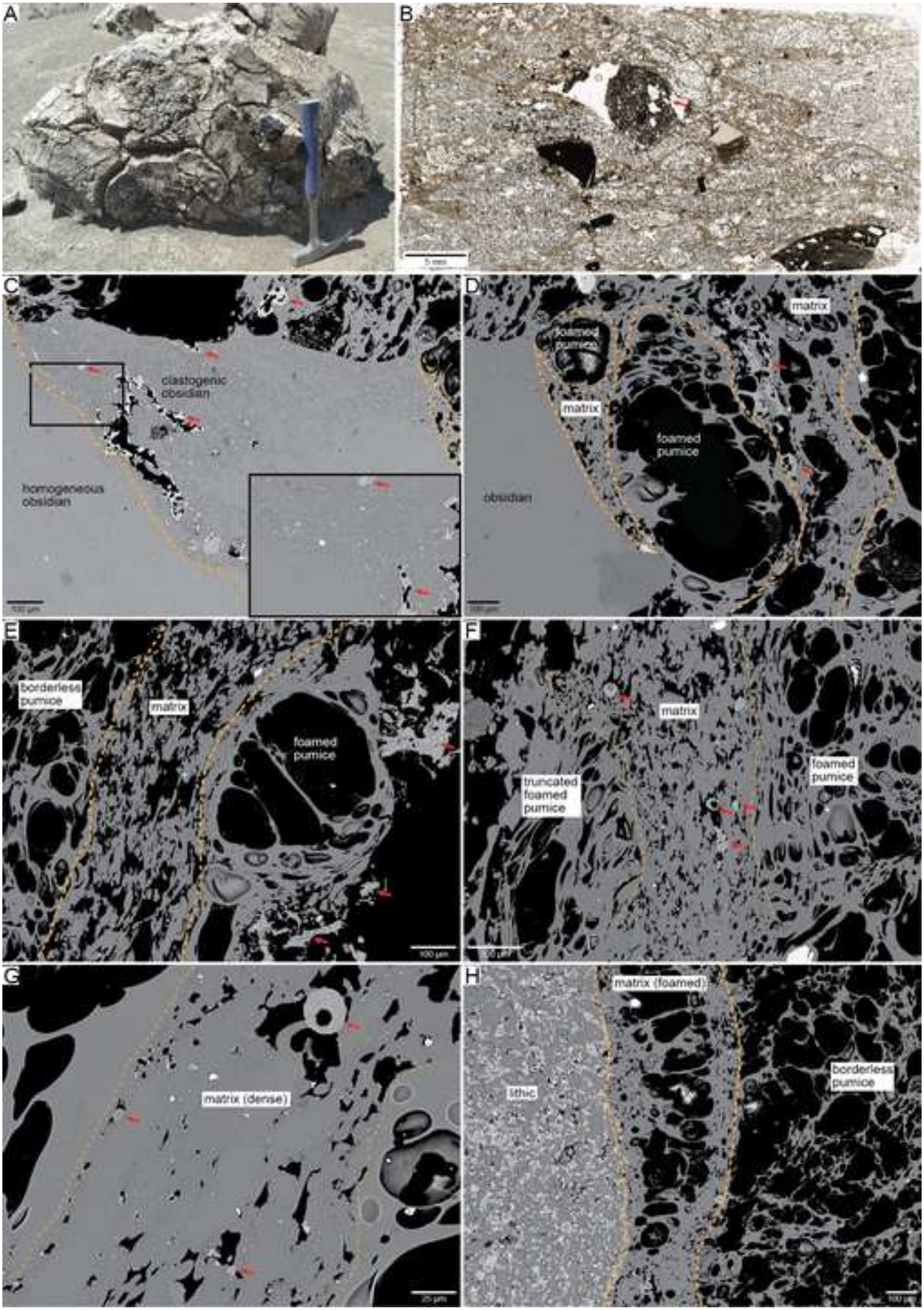
A
B
5 mm
C
clastogenic obsidian
homogeneous obsidian
D
foamed pumice
matrix
foamed pumice
obsidian
matrix
E
borderless pumice
matrix
foamed pumice
F
matrix
truncated foamed pumice
foamed pumice
G
matrix (dense)
25 µm
H
matrix (foamed)
lithic
borderless pumice

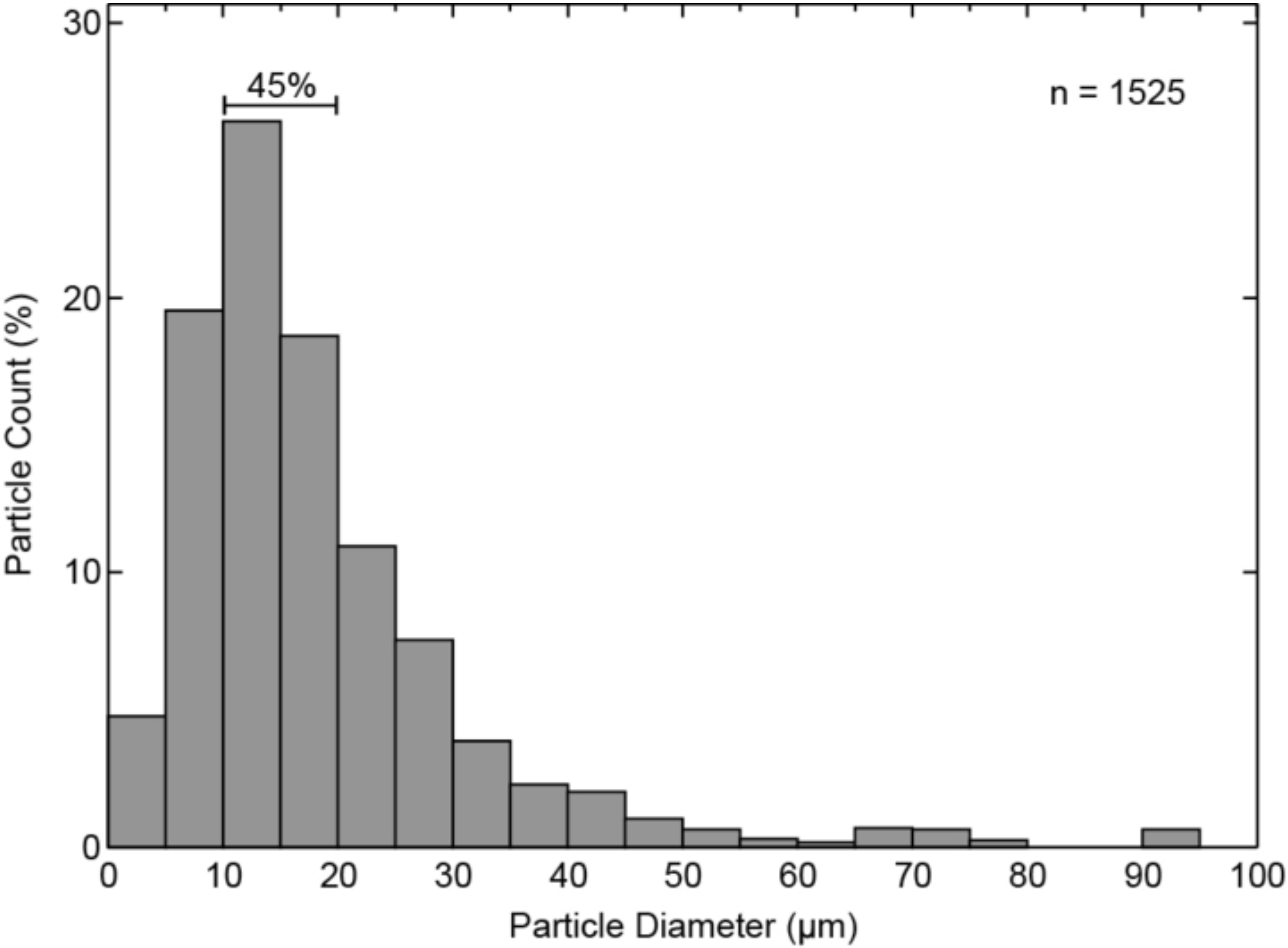
45%
n = 1525
Particle Count (%)
0
10
20
30
0
10
20
30
40
50
60
70
80
90
100
Particle Diameter (µm)

Fig.6

Click here to access/download;Figure;Schipper et al. R1-Fig.6.jpg

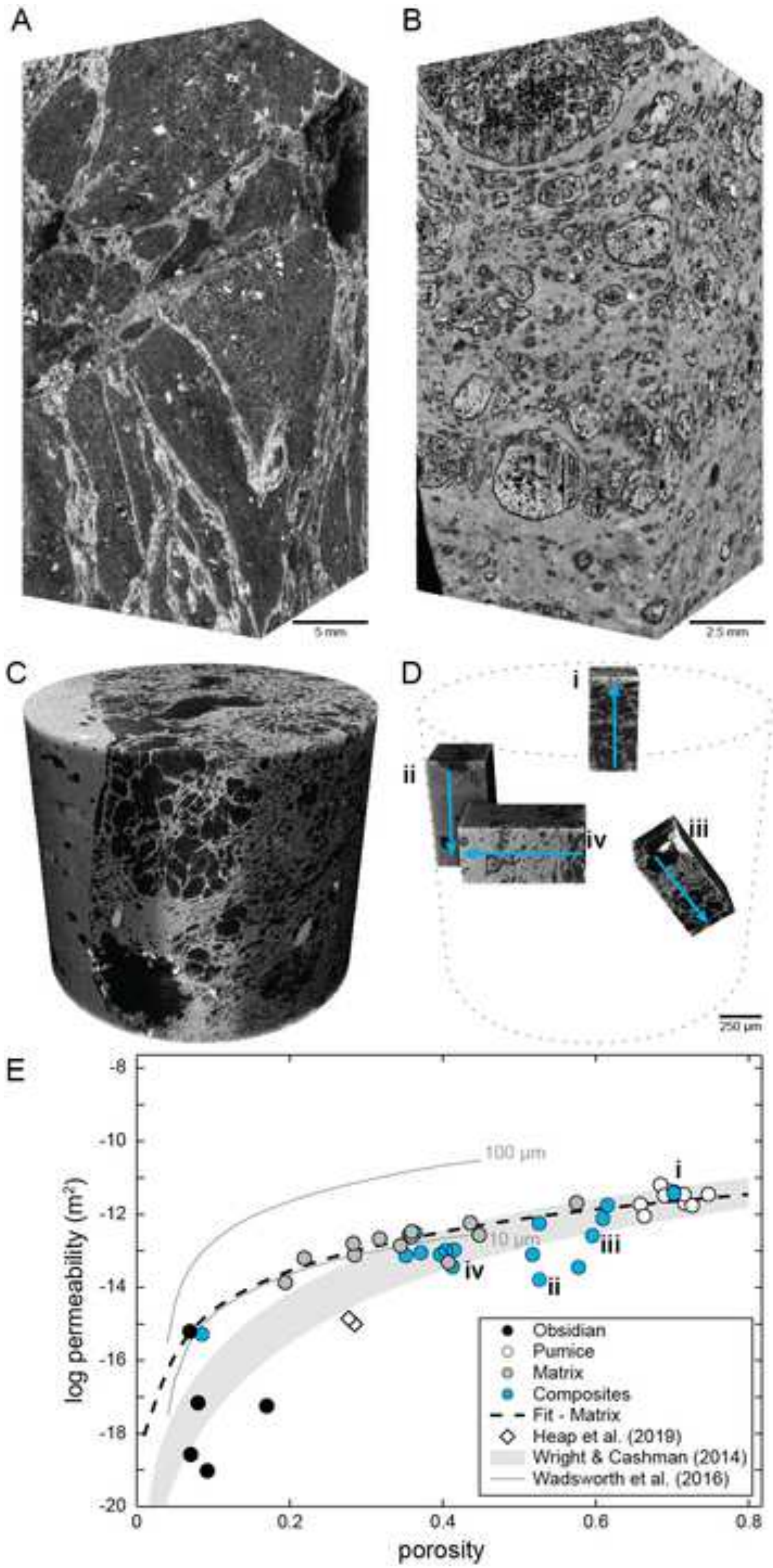

Fig.7

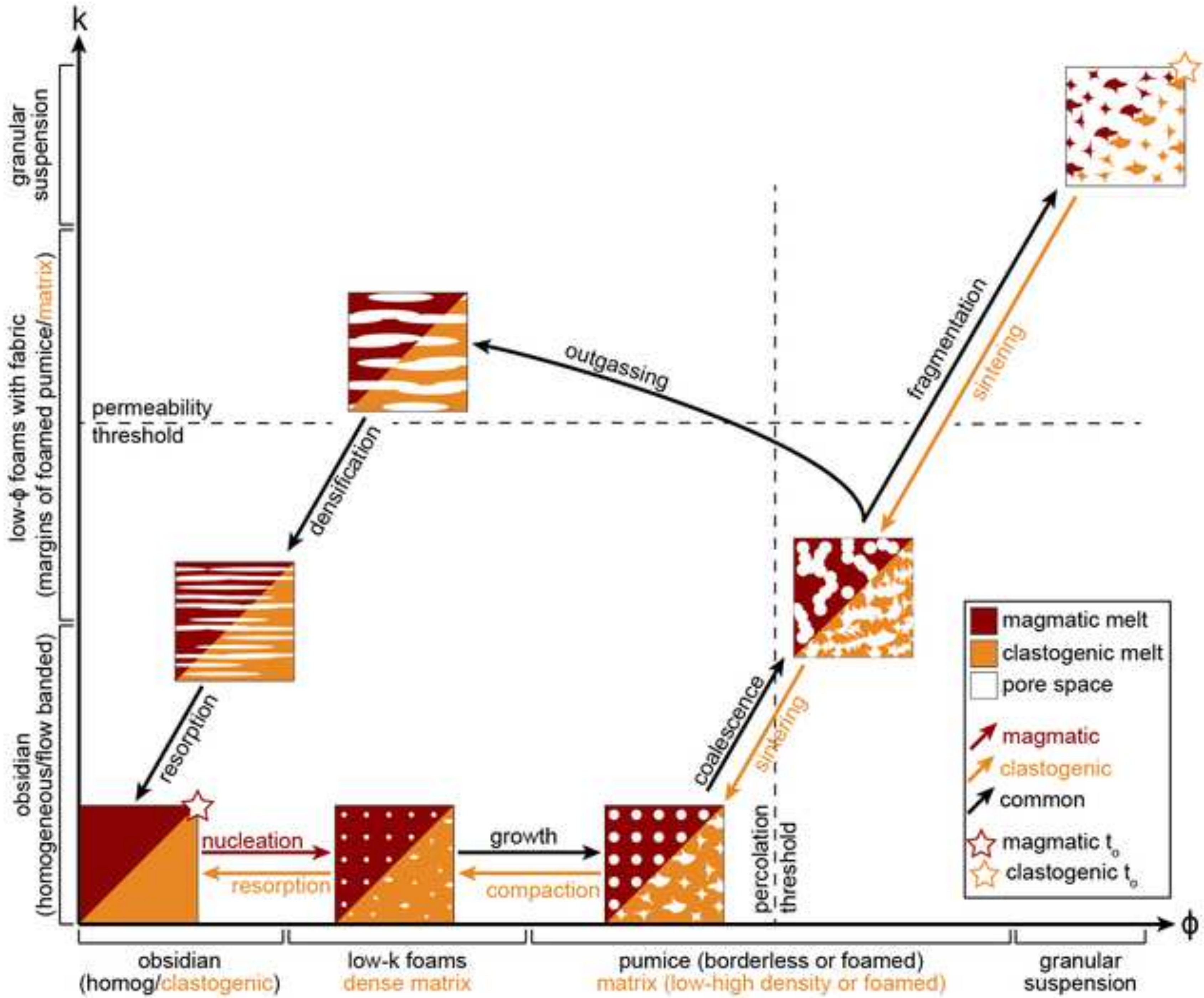
k
ϕ
granular suspension
low-ϕ foams with fabric (margins of foamed pumice/matrix)
obsidian (homogeneous/flow banded)
permeability threshold
percolation threshold
outgassing
fragmentation
sintering
densification
resorption
coalescence
sintering
nucleation
resorption
growth
compaction
magmatic melt
clastogenic melt
pore space
magmatic
clastogenic
common
magmatic t_o
clastogenic t_o
obsidian (homog/clastogenic)
low-k foams dense matrix
pumice (borderless or foamed) matrix (low-high density or foamed)
granular suspension

Fig.8

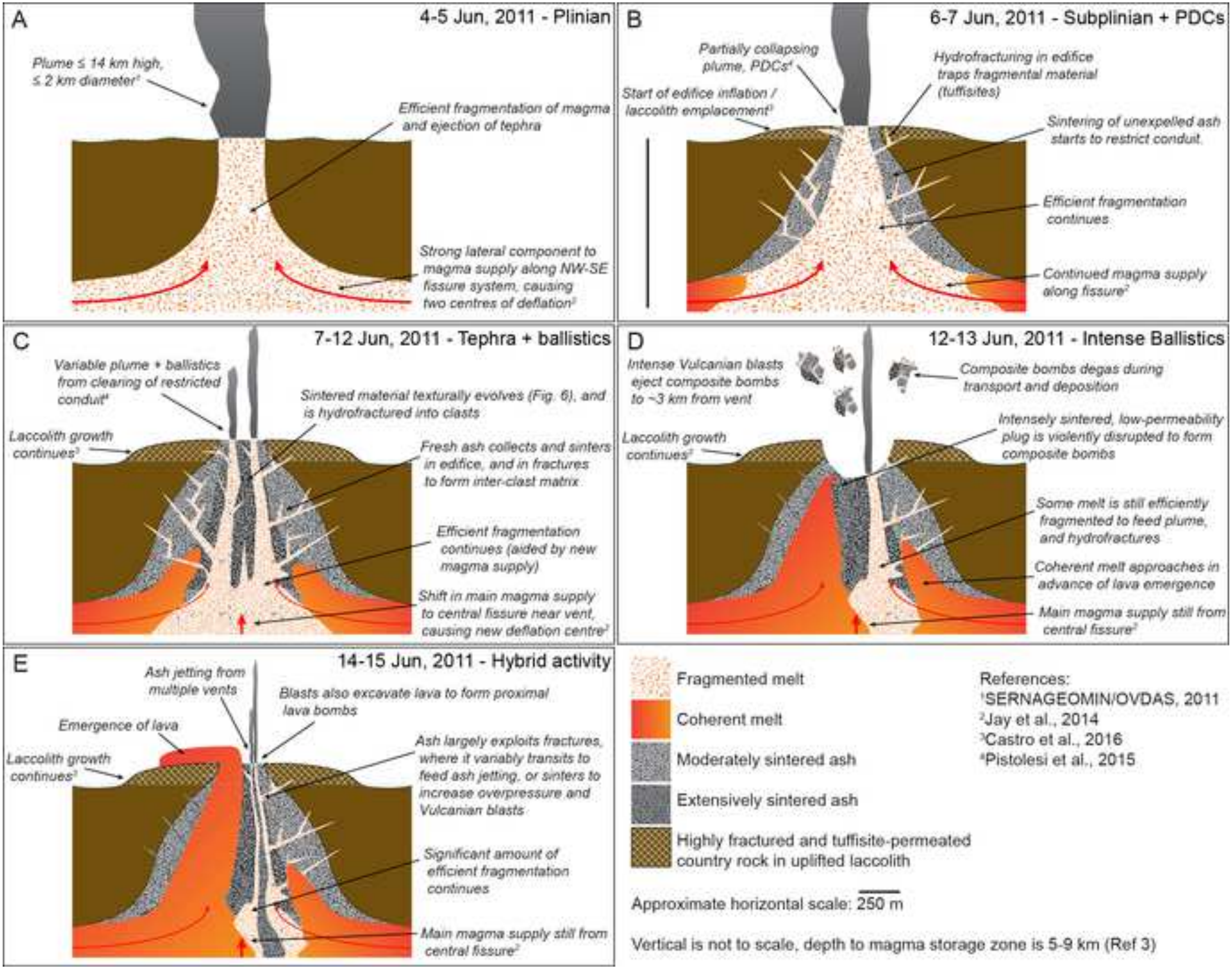
A
4-5 Jun, 2011 - Plinian
Plume ≤ 14 km high, ≤ 2 km diameter[1]
Efficient fragmentation of magma and ejection of tephra
Strong lateral component to magma supply along NW-SE fissure system, causing two centres of deflation[2]
B
6-7 Jun, 2011 - Subplinian + PDCs
Partially collapsing plume, PDCs[4]
Hydrofracturing in edifice traps fragmental material (tuffisites)
Start of edifice inflation / laccolith emplacement[3]
Sintering of unexpelled ash starts to restrict conduit
Efficient fragmentation continues
Continued magma supply along fissure[2]
C
7-12 Jun, 2011 - Tephra + ballistics
Variable plume + ballistics from clearing of restricted conduit[4]
Sintered material texturally evolves (Fig. 6), and is hydrofractured into clasts
Laccolith growth continues[3]
Fresh ash collects and sinters in edifice, and in fractures to form inter-clast matrix
Efficient fragmentation continues (aided by new magma supply)
Shift in main magma supply to central fissure near vent, causing new deflation centre[2]
D
12-13 Jun, 2011 - Intense Ballistics
Intense Vulcanian blasts eject composite bombs to ~3 km from vent
Composite bombs degas during transport and deposition
Intensely sintered, low-permeability plug is violently disrupted to form composite bombs
Laccolith growth continues[3]
Some melt is still efficiently fragmented to feed plume, and hydrofractures
Coherent melt approaches in advance of lava emergence
Main magma supply still from central fissure[2]
E
14-15 Jun, 2011 - Hybrid activity
Ash jetting from multiple vents
Blasts also excavate lava to form proximal lava bombs
Emergence of lava
Laccolith growth continues[3]
Ash largely exploits fractures, where it variably transits to feed ash jetting, or sinters to increase overpressure and Vulcanian blasts
Significant amount of efficient fragmentation continues
Main magma supply still from central fissure[2]
Fragmented melt
Coherent melt
Moderately sintered ash
Extensively sintered ash
Highly fractured and tuffisite-permeated country rock in uplifted laccolith
References:
[1]SERNAGEOMIN/OVDAS, 2011
[2]Jay et al., 2014
[3]Castro et al., 2016
[4]Pistolesi et al., 2015
Approximate horizontal scale: 250 m
Vertical is not to scale, depth to magma storage zone is 5-9 km (Ref 3)

Table 1

Table 1. Composite Bomb descriptions and analysis types

Name	Lat	Long	Elev	Comment	Figure	Hand Sample	Thin Section	SEM	CT Low	CT High
P13-B01	-40.510	-72.177	1563	Decimetric fragments of obsidian composite around ~2.5 m impact crater						
P13-B10	-40.524	-72.148	1648	Pumice-dominated composite bomb with grey matrix and black foamed interior						
011-IS	-40.524	-72.147	1645	Large obsidian bomb, with vesicular flow bands	3J	X	X	X		
P13-B12	-40.524	-72.147	1645	Proximal obsidian bomb ("crat")		X	X	X		
P13-B13	-40.525	-72.147	1643	Obsidian-dominated composite bomb. Appears homogeneous in hand sample, composite in thin section ("mini")		X	X	X		
P13-B19	-40.509	-72.156	1565	Decimetric fragments of pumice- and obsidian-dominated composite material around ~1.7 m crater		X				
P13-B20	-40.509	-72.156	1567	Decimetric fragments of obsidian and pumice around ~2.1 m crater						
P13-B21	-40.509	-72.156	1567	~4.2 m impact crater, with ~50 cm pumice-dominated composite bomb (fragment), light grey matrix						
P13-B24	-40.509	-72.156	1563	Decimetric fragments of pumice-dominated, grey-matrix composite bomb at rim of >5 m diameter impact crater						
P13-B25	-40.509	-72.155	1563	~40 cm composite bomb fragment with mingled obsidian bands and in-situ foamed clasts						
P13-B26	-40.510	-72.155	1561	~4.3 m impact crater with large (<60 cm) fragments of pumice-dominated composite bomb with light grey matrix						
P13-B27	-40.510	-72.155	1560	~6 m impact crater with decimetric fragments of obsidian and pumice breccia						
P13-B32	-40.510	-72.156	1557	Fragments of obsidian-dominated composite bomb at edge of ~2 m impact crater		X				
P13-B35	-40.510	-72.157	1532	Large, intact, extensively breadcrusted, pumice-dominated composite bomb, with obsidian clasts <15 cm	3C					
P13-B39	-40.510	-72.156	1544	Composite bomb with large borderless pumice separated by vein of red matrix with pumice fiamme and obsidian						
P13-B42	-40.510	-72.155	1533	Pumice-dominated composite bomb with angular obsdidian clasts, light orange matrix and no defined fabric						
P13-B43	-40.510	-72.155	1534	Composite bomb, appears lava-like on surface, but with large glassy obsidian clast at centre						
P13-B44	-40.510	-72.155	1531	~1.5 m composite bomb fragment in ~4.5 m crater. Pumice-dominated, with many in-situ foamed and obsidian clasts						
P13-B49	-40.504	-72.155	1542	~30 cm dense obsidian-dominated composite bomb, matrix and lithic in isolated domains						
P13-B50	-40.505	-72.155	1528	~50 cm obsidian-dominated bomb fragment at rim of ~4 m crater mantled by pumice fragments		X	X	X		
P13-B51	-40.505	-72.153	1515	~20 cm composite fragments with ~6 m crater. Sharp boundary between obsidian-dominated and pumice-dominated						
P13-B53	-40.505	-72.152	1503	Composite bomb dominated by borderles fiamme pumice, orange matrix, striking ~4 cm obsidian clast, breadcrusted	3D	X				
P13-B55	-40.507	-72.154	1562	Coarse pumice-dominated composite, mixture of borderless pumice <50 cm and in situ foamed to ~4 cm. Reddish matrix.						
P13-B57	-40.510	-72.155	1527	~1 m pumice-dominated compoiste with light orange matrix and poorly defined fabric						
P13-B58	-40.510	-72.155	1526	Matrix-dominated composite with abundant in situ foamed pumice. Colour-banded matrix from grey-red	3I, 5B	X	X	X	X	
P13-B59	-40.510	-72.154	1506	~1 m obsidian bomb with no obvious matrix but lithic and in situ foamed pumice						
P13-B61	-40.510	-72.151	1452	~60 cm composite dominated by borderless pumice, little matrix, and reddish interior cavity						
P14-038	-40.513	-72.157	1532	Large, breadcrusted composite. Pumice dominated but with large angular obsidian to ~4 cm and grey matrix	4	X	X	X		
P14-B02	-40.510	-72.158	1496	Large mid-density composite bombs with all clast types, variable fabric, and red oxidized matrix	3E, 5C-D	X	X	X	X	X
P14-B05	?	?	?	Obsidian-dominated composite bomb with irregular domains of grey matrix		X				
P14-B52	?	?	?	Obsidian-cominated composite, no obvious matrix, in-situ foamed pumice ~5 cm		X	X	X		
P14-PIC448	?	?	?	Pumice-dominated composite bomb with poorly-defined fabric. Brownish-red matrix, and occasional obsidian						
P14-PIC41	-40.522	-72.148	1616	Dense lava bomb	3B	X	X	X		
P14-PIC46	-40.521	-72.148	1602	Dark, dense (composite?) lava bomb						
P14-PIC40	-40.522	-72.148	1633	Dense lava bomb						
P14-PIC42	-40.521	-72.148	1600	Dense lava bomb	3A					
P14-PIC51	-40.521	-72.149	1591	Obsidian Composite bomb containing lithic clasts						
P14-PIC52	-40.521	-72.149	1581	Large, pumice-dominated composite bomb with dark oxidized interior		X	X	X		
P14-PIC554	-40.524	-72.147	1648	Pumice-dominated composite bomb with irregular oxidation patterns						
P14-PIC555	-40.524	-72.147	1648	Moderaly vesicular lava bomb. Oxidized on one surface.						
P14-PIC556	-40.524	-72.147	1646	Irregular lava bombs, moderately vesicular.						
P14-PIC557	-40.524	-72.147	1650	Moderaly vesicular lava bomb. Oxidized on one surface.						
P14-PIC558	-40.524	-72.147	1648	Pumice-dominated composite bomb with red oxidized central cavity						
P14-PIC559	-40.524	-72.147	1643	Fractured, pumice-dominated composite bombs with dark/oxidized cavities						
P14-PIC560	-40.524	-72.146	1642	Pumice-dominated composite bomb with red oxizidized matrix						
P14-PIC561	-40.524	-72.146	1643	Pumice bomb, with oxidized cavity at interior						
P14-PIC562	-40.524	-72.146	1645	Large lava bomb. Several internal cavities, slight surface oxidation.						
P14-PIC565	-40.523	-72.146	1650	Moderaly vesicular lava bomb. Oxidized on one surface. Large interior cavity.						
P16-B01	-40.508	-72.156	1610	1.5 m diameter, pumice-dominated, breadcrusted composite bomb						
P16-B02	-40.508	-72.156	1609	~80 cm diameter, obsidian+pumice, breadcrusted composite bomb						
P16-B03	-40.509	-72.156	1567	Fragments of pumice-dominated composite bomb with fabric and pink oxidized matrix						
P16-B04	-40.509	-72.156	1566	Fragments of pumice-dominated composite bomb with spase obsidian to ~3 cm						
P16-B05	-40.513	-72.156	1535	Pumice-dominated composite bomb fragments with glassy in-situ foamed clasts to ~4 cm						
P16-B06	-40.513	-72.156	1535	Obsidian, and frothed obsidian banded composite bomb (concertina)						
P16-B07	-40.512	-72.156	1531	Pumice-fiamme dominated composite bomb with pink matrix and rare obsidian to ~5 cm	3F, 5A	X	X	X	X	
P16-B09	-40.511	-72.153	1486	High-density, obsidian-dominated composite bomb with orange matrix	3H	X	X	X	X	
P16-B10	-40.512	-72.150	1483	High-density, glassy, obsidian-dominated composite bomb with lithics but no obvious matrix		X	X	X	X	
P16-B11	-40.512	-72.150	1470	High-density composite with banded texture, rich in borderless obsidian, small in-situ foaming		X	X	X	X	
P16-B12	-40.512	-72.150	1444	Moderate density pumice fiamme composite with occasional obsidian to ~3 cm. Breadcrusted.		X	X			
P16-B13	-40.512	-72.149	1456	Very high-denisty, obsidian-dominated composite with abundant lava-like lithic clasts		X	X	X	X	
P16-B14	-40.512	-72.149	1460	Very high-denisty, obsidian composite with grey matrix		X	X		X	
P16-B15	-40.511	-72.149	1474	Composite of large borderless pumice clasts with angular and platey obsidian. No obvious matrix						
P16-B16	-40.510	-72.155	1526	Matrix-dominated composite with many in-situ foamed clasts. (pebble/honeycomb bomb)		X	X	X	X	
P16-B17	-40.519	-72.166	1503	Matrix-dominated composite with many in-sity foamed domains that are v. low density and glassy		X	X		X	
P16-B18	-40.519	-72.166	1501	High-denisty, obsidian-dominated composite with thin tendrils of oxidized matrix		X			X	
P16-B19	-40.519	-72.166	1502	Pumice-dominated composite, lacking fabric, orange matrix.						

P16-B20	-40.519	-72.166	1508	Composite with wide variety of angular clasts pumice>obsidian>lithics. Light pink matix, no fabric.	3G	X	X	X	X
P16-B21	-40.520	-72.166	1502	Variably-foamed, banded, obsidian+foam composite.		X	X	X	X
P16-B22	-40.521	-72.168	1508	Slightly breadcrusted, punice-dominated composite. Grey matrix. Chaotic fabric.					
P16-B23	-40.521	-72.168	1510	Breadcrusted, Pumice-dominated composite with chaotic fabric and outer obsidian rind.					